4-2022

Design and Optimization of An Electron Cyclotron Resonance Thruster

Austen Thomas
Western Michigan University

DESIGN AND OPTIMIZATION OF AN ELECTRON CYCLOTRON RESONANCE THRUSTER

Austen Jacob Thomas, M.S.

Western Michigan University, 2022

Presented in this work is the process in the design and optimization of a coaxial electron cyclotron resonance thruster. Electron cyclotron resonance thrusters are novel microwave-based thrusters which possess select technological advantages over mature electric propulsion concepts such as being electrodeless and only requiring a single power source. The thruster constructed in this work is a coaxial configuration and is termed the Western electron cyclotron resonance thruster. Thruster dimensions were optimized based on past experimentation completed with ECR thrusters. In an attempt to enhance the microwave plasma coupling of the coaxial thruster design three different antenna configurations were considered: a monopole as used in previous studies, a ring antenna, and a helical antenna. Only the monopole and helical antenna went through experimental verification.

The characterization of the thruster was completed at Western Michigan University through a series of experiments and is presented here. These include the use of a variety of plasma diagnostic equipment consisting of a Langmuir probe, Faraday cup, and a retarding potential analyzer. The experiments allow the plasma properties and performance metrics such as thrust, specific impulse, and thruster efficiencies to be calculated. The thruster displayed performance on par with other first design iterations of electron cyclotron resonance thrusters; although, it did not

reach the maximum performance obtained from more recent designs. From results obtained during experiments on the initial thruster design, a second thruster design was developed with select changes and improvements. Future investigations may include studies on microwave plasma coupling and magnetic nozzle physics. It is believed that electron cyclotron resonance thrusters possess the capability to play a significant role in the space industry and aid in its future development.

DESIGN AND OPTIMIZATION OF AN ELECTRON CYCLOTRON RESONANCE THRUSTER

by

Austen Jacob Thomas

A thesis submitted to the Graduate College
in partial fulfillment of the requirements
for the degree of Master of Science in Aerospace Engineering
Western Michigan University
April 2022

Thesis Committee:

Kristina Lemmer, Ph.D., Chair
Muralidhar Ghantasala, Ph.D.
Michael McDonald, Ph.D.

ACKNOWLEDGMENTS

Throughout my studies I have had the support of numerous individuals without whom this would not have been possible. First, I would like to thank my mother and father who have supported me not just through my education but throughout my life. Without them I would not be the person I am today. I must also thank my uncle, Mike Ryall, who aided in the fabrication of the thruster and made its testing possible. I would not have been able to complete this work without my professor Dr. Kristina Lemmer and lab mates, who have provided valuable information, guidance, and have assisted me during the testing of the thruster. I must also thank Jim Cotton who has been extremely helpful in providing knowledge and equipment for this work. Lastly, the support of my girlfriend Sophia for putting up with late nights and my relentless talking of physics. I am thankful for the opportunity given to me to complete this work and am looking forward to what the future holds.

Austen Jacob Thomas

TABLE OF CONTENTS

Table of Contents—Continued

LIST OF TABLES

LIST OF FIGURES

CHAPTER 1

INTRODUCTION

1.1 Background

Space exploration and the space industry has been rapidly expanding over the past decade with increasing satellite launches every year. Historically space propulsion systems have relied on chemical propulsion to achieve the necessary maneuvers. Over time satellite propulsion systems have become increasingly more reliant on electric propulsion (EP) over chemical propulsion for in space applications. EP is a class of space propulsion utilizing electrical energy to generate thrust. The concept of using electrical energy to accelerate a propellant has been around since the early 1900's pioneered by famed scientists Robert Goddard and Konstantin Tsiolkovsky. Interest in EP devices became more relevant in the 1950's but was outpaced by chemical propulsion because of low thrust capabilities and technical requirements [1]. Significant developments were made in the 1990's allowing for EP devices to make substantial technological growth including the launch of the Xenon Ion Propulsion System (XIPS) and NASA Solar Electric Propulsion Technology Applications Readiness (NSTAR) ion thruster [2]. These developments allowed EP devices to become relevant for missions involving low thrust maneuvers. The devices have become capable of performing tasks such as spacecraft orientation, orbital shifts, drag combat, and more recently as a primary propulsion system for long duration missions.

Electric and chemical propulsion each operate on the same principle of conservation of momentum. To produce a change in velocity and therefore forward motion, mass from the vehicle must be accelerated away. The force and therefore thrust T exerted on a spacecraft from ejecting propellent is equivalent to the mass of the spacecraft M multiplied by its change in velocity v.

$$T = M\frac{dv}{dt} \tag{1.1}$$

While both classes of propulsion operate on the same principal, EP possesses significant advantages over chemical propulsion. A chemical rocket is limited by the energy release available within the propellant. Chemical rockets utilize the energy within the molecular bonds by creating a chemical reaction releasing the energy through combustion processes. Hot gases are then expanded through a nozzle where the thermal energy is converted into directed kinetic energy creating a high level of thrust. While chemical rockets can achieve high levels of thrust, they are restricted to a specific impulse, I_{sp}, under 500 s. Where I_{sp} is a measure of how efficiently thrust is produced for a given amount of propellant. EP devices however are not limited by the energy available in the propellant, but by the power deposited into the propellant. Allowing the I_{sp} to reach over 10,000 s and generate high exhaust velocities [2]. To gain an understanding of the effectiveness of a propulsion system, equation (1.1) can be used to obtain the Tsiolkovsky Rocket Equation. As a propulsion system is operating, it is expelling propellant and the overall spacecraft mass is changing as a function of time $M(t) = m_d + m_p$ where m_d is the delivered mass of the spacecraft and m_p is the mass of the propellant. The thrust created is equivalent to the time rate of change of the momentum of the ejected propellant mass in the opposite direction.

$$T = -v_{ex}\frac{dm_p}{dt} \tag{1.2}$$

Where v_{ex} is the exhaust velocity of the propellant. By equating (1.1) and (1.2) the force exerted on the spacecraft by the propellent is

$$M\frac{dv}{dt} = -v_{ex}\frac{dm_p}{dt} \tag{1.3}$$

Equation (1.3) can be maniupulated and integrated resulting in equation (1.4).

$$\int_{v_i}^{v_f} dv = -v_{ex} \int_{m_{d+m_p}}^{m_d} \frac{dM}{M} \tag{1.4}$$

This integration then yields the Tsiolkovsky Rocket Equation.

$$\Delta v = I_{sp} g_0 \ln\left(\frac{m_0}{m_f}\right) \tag{1.5}$$

The Tsiolkovsky equation shows Δv, the change in velocity, is only dependent on the mass ratio and I_{sp}; therefore, the most effective way to increase a spacecraft Δv is by increasing the I_{sp} [2]. Δv describes a spacecrafts ability to perform a particular maneuver or achieve a mission. Missions which require a high Δv are better suited for EP devices because of their capability of achieving high I_{sp} unlike conventional chemical propulsion systems. As an added benefit EP systems also carry significantly less propellant than a chemical system, greatly reducing the overall mass. EP devices vary in I_{sp} and thrust depending on the methods used to create thrust. A variety of these EP classes are discussed in the following section.

1.2 Electric Propulsion Thrusters Classes

EP thrusters have typically fallen under three categories electrothermal, electrostatic, and electromagnetic. A fourth class of thruster utilizing electromagnetic waves to ionize a gas has again gained recent attention and is discussed in section 1.3. Each category relies on different methods for ionizing a gas and accelerating the plasma resulting in the generation of thrust. In all categories electric power is used to heat or ionize a propellant. As discussed above EP devices possess greater exhaust velocities allowing for a high I_{sp} at low thrust levels when compared to chemical propulsion. Each category of EP possesses select advantages and disadvantages; some devices possess greater I_{sp} at the expense of thrust. While others generate greater levels of thrust

at lower I_{sp}. There are numerous challenges still facing EP which require research. To name a few, improvement of I_{sp} in EP devices, small satellite propulsion systems, lifetime of plasma thrusters, plasma cathode failures, etc [3]. The following subsections will provide a brief description of the above-mentioned classes of EP.

1.2.1 Electrothermal Propulsion

Electrothermal thrusters use electrical energy to heat propellant that is subsequently expanded through a nozzle. The electrical power delivered to the propellant is accomplished by a resistively heated surface, an arc, or by electromagnetic radiation. These devices include resistojects and arcjets. In a resistojet, propellant is heated by passing a gas through a resistively heated surface such as coils or wires aligned parallel to the flow, prior to entering a nozzle [4]. The heated gas is then expanded through the nozzle converting the thermal energy into kinetic energy increasing the exhaust velocity, but limits the I_{sp} to low levels ~ 500 s. An arcjet heats the propellant by passing it through a high current arc leading up to a nozzle, where the weakly ionized gas is allowed to expand. Plasma effects have little effect on the exhaust velocity because of the weakly ionized propellant, limiting the I_{sp} to less than 700 s [2]. Displayed in Figure 1 are the resistojet and arcjet concepts.

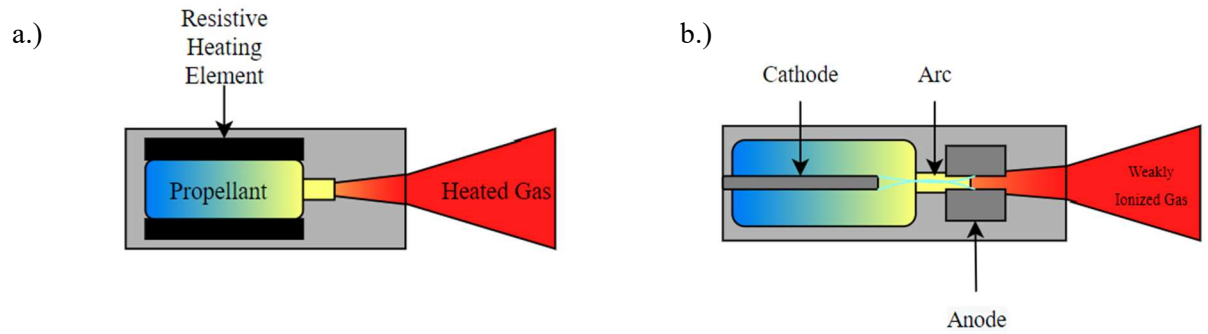

Figure 1: a). Resitojet and b.) Arcjet basic operation and geometry.

1.2.2 Electrostatic Propulsion

Electrostatic propulsion accelerates an ionized propellant through the application of electrostatic forces. An electric field is created through the application of a large electric potential accelerating the ionized propellant. Magnetic fields can also be applied aiding in the ionization process or confinement of the plasma. Two of the primary electrostatic thrusters are gridded ion thrusters (GIT) and hall effect thrusters (HET). GIT's use electrically biased grids to electrostaticlly accelerate ions from the plasma. GIT's posses an arrary of ionization techniques including but not limited to electron bombardment and the electron cyclotron resonance (ECR) method. GIT's achieve the highest upper limit of I_{sp} for electric propulsion devices with the potential to reach 10,000 s [2]. HET's utilize a cross field structure to ionize a gas and accelerate ions. An electric field is established perpendicular to a magentic field allowing the electrostatic acceleration of ions. The magnetic field is used to contain electrons for use in ionizing the injected propellant. HET's posses I_{sp} around ~1200-2500 s [2]. Illustrated in Figure 2 are both the GIT and HET concepts.

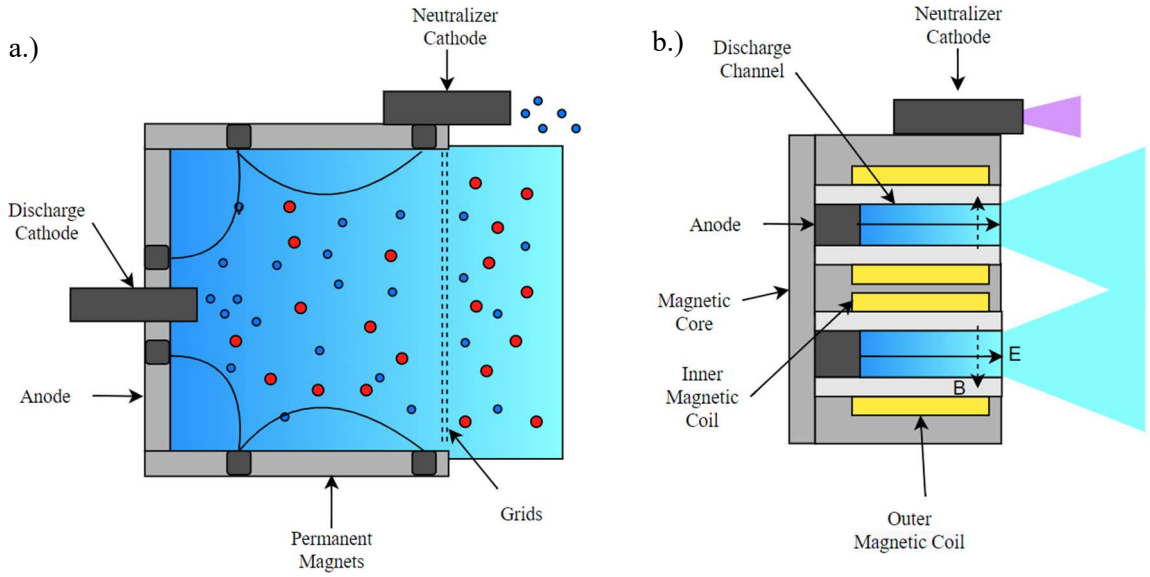

Figure 2: a.) Gridded ion thrust and b.) Hall effect thruster basic operation and geometry.

1.2.3 Electromagnetic Propulsion

Electromagnetic propulsion utilizes either internal or external magnetic fields with electrical currents to accelerate an ionized propellant. An electromagnetic thruster produces thrust via the Lorentz force. Two electromagnetic thruster devices are the Magnetoplasmadynamic (MPD) thrusters and pulsed plasma thrusters (PPT). MPD thrusters operate most efficiently at high power levels generating high thrust and I_{sp}. This is accomplished by the thruster utilizing a high current arc to ionize a propellant allowing the Lorentz force to accelerate the ionized propellant. A PPT operates by creating a pulsed discharge ionizing a portion of a solid propellant. Electromagnetic effects within the pulse then accelerate the ions [2]. Figure 3 displays the PPT and MPD thruster concepts.

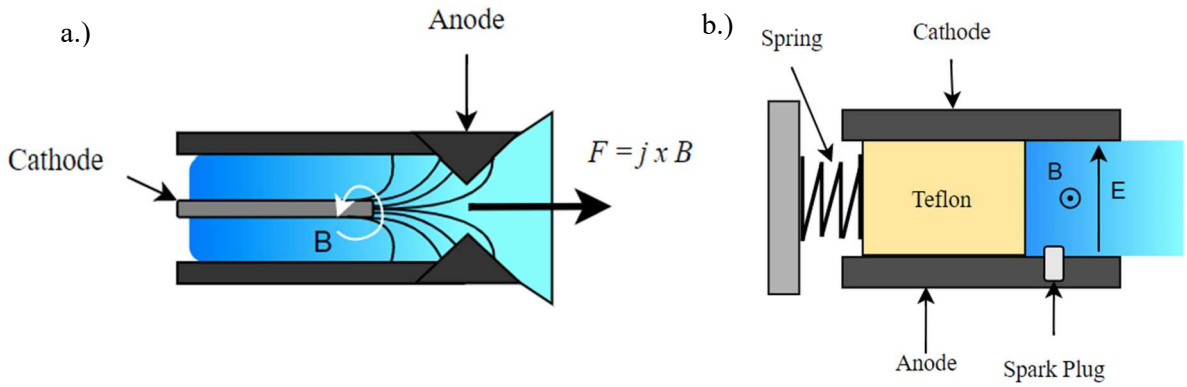

Figure 3: a.) Magnetoplasmadynamic thruster and b.) Pulsed plasma thruster basic operation and geometry.

1.3 Radio Frequency and Microwave Thrusters

As mentioned previously a fourth class of electric propulsion thrusters are wave driven thrusters. With recent developments in radio frequency (RF) and microwave (MW) technologies, wave driven thrusters have gained increased attention for unique advantages over conventional electric propulsion technologies. RF and MW thrusters utilize electromagnetic waves to excite free electrons in a neutral gas through numerous methods. Two thruster designs, each utilizing a

different method for plasma generation, are Helicon plasma thrusters (HPT) and ECR thrusters these concepts are illustrated below in Figure 4.

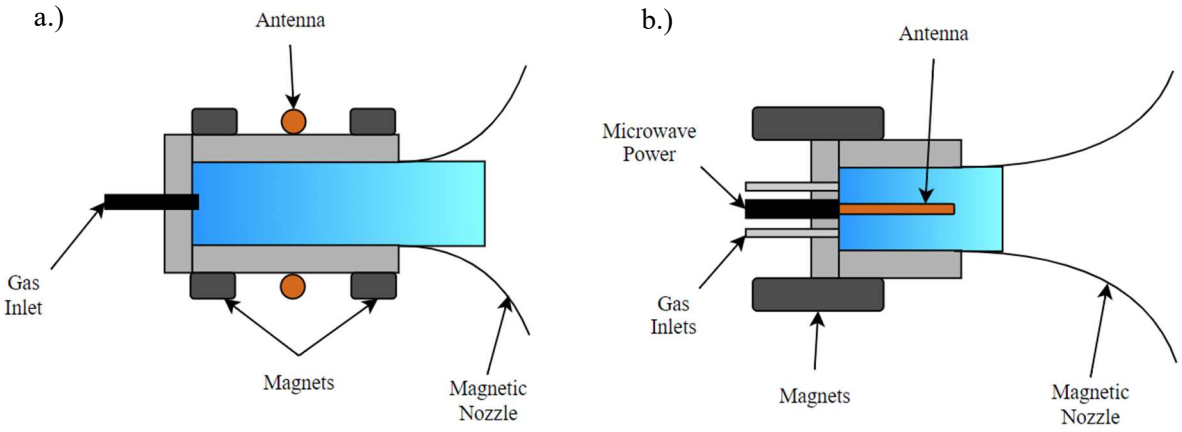

Figure 4: a.) Helicon plasma thruster and b.) electron cyclotron resonance thruster basic operation and geometry.

The most substantial benefit of this thruster class is the absence of electrodes. Conventional EP technologies all require some use of electrodes to ionize or accelerate a plasma. Increasing the power deposited into the plasma in thrusters such as GITs and HETs leads to an increase in erosion and early failure of the electrodes. HPT and ECR thrusters eliminate the need for electrodes using instead electromagnetic waves to generate the plasma. This increases the lifetime of these thruster concepts. The elimination of electrodes also adds the capability of using alternative propellants such as molecular gases without the risk of contamination of electrodes. Additionally, HPT and ECR thruster configurations only require a single power source in the form of RF or MW power in some cases.

1.4 Motivation

As EP technologies continue to advance, they become more applicable to a variety of space-based applications. New technologies and thruster designs will continue to be developed offering potential benefits compared to mature technologies such as HETs and GITs. One such device is ECR thrusters; these devices are electrodeless magnetic nozzle thrusters utilizing both

electric and magnetic fields to accelerate a plasma. Currently, ECR thrusters are at an early technology readiness level (TRL). The physics are not well understood in some aspects, but working prototypes have are being developed and tested. Wave driven thrusters such as ECR thrusters have not been capable of matching the performance and efficiencies that are possible in the more mature technologies. If substantial improvements in performance can be made ECR thrusters offer potential advantages mature electric propulsion technologies do not possess. A list is presented below: [5]

- Lower reoccurring cost per unit
- Higher reliability
- Longer lifetime
- Magnetic thrust vectoring
- Ambipolar acceleration
- Completely compatible with all propellants
- Electrically neutral plume
- Few components
- Scalability

The focus of this thesis is the design of a small-scale low power ECR thruster capable of efficiencies on par with first iteration designs and possibly to exceed those limits. Additionally, the ECR thruster constructed in this thesis will add to the database available for information on ECR thrusters. These thruster concepts require significant improvements if they are to play a role in space propulsion applications; this work will aid in that endeavor.

1.5 Thesis Outline

The contents of this thesis are organized as follows. Chapter 2 discusses the physics and operating principles of an ECR thruster. Chapter 3 presents the thruster design based on the physics and operating principles presented in Chapter 2, along with past experimental results. Chapter 4 discusses the facilities and experimental setup used in characterizing the thruster design, including the vacuum system, plasma diagnostic equipment, microwave, and gas flow set-ups. Chapter 5 discusses the experimental results obtained with a series of plasma diagnostics and a discussion of the results obtained. Chapter 5 also discusses the optimized second thruster design based on the results obtained from the initial concept. Chapter 6 concludes the study with a summary of the work completed and potential future work.

CHAPTER 2

PHYSICS AND OPERATING PRINCIPLE

2.1 Plasma

Plasma is a quasi-neutral gas consisting of charged and neutral particles that exhibits collective behavior and is affected by electrostatic and magnetic forces. The composition of plasma provides it the ability to be manipulated, making it useful in EP devices. Numerous methods are available for generating plasma. The most common methods are electron bombardment, high current arc discharge, and wave driven discharges. Electron bombardment consists of high energy collisions constantly freeing bound electrons from neutral atoms creating more free electrons. A single ionizing collision results in two negatively charged electrons and a positively charged ion generating the plasma. An arc discharge plasma is formed by flowing electric current through a neutral gas. This typically occurs by applying a voltage between an anode and cathode creating a high current electric arc. Wave driven discharges can be generated by RF or MW electromagnetic waves. An RF plasma can be created by RF currents being circulated through either an antenna or coil. The RF current in the coil or antenna induces a time varying magnetic field which in turn creates a time varying electric field capable of accelerating free electrons creating collisional ionization generating the plasma [2]. Finally, a common method for generating a microwave plasma is by ECR. Presented in this work is a wave driven ECR plasma thruster, this method of plasma generation is discussed in the following section.

2.2 Electron Cyclotron Resonance

ECR is the phenomena where electrons are continually heated through electromagnetic wave coupling within a static magnetic field. As electrons are heated, they continually gain gyrokinetic energy as they rotate around magnetic field lines. The increase in energy leads to high

energy collisions of charged particles producing the ionized gas. Electrons gyrate around the magnetic field lines with a frequency ω_{ce} where e is the elementary charge, m_e is the mass of an electron, and B is the magnetic field strength.

$$\omega_{ce} = \frac{eB}{m_e} \tag{2.1}$$

The ECR region is established when the electron cyclotron frequency coincides with the electromagnetic wave frequency ω_{rf}. A microwave frequency of 2.45 GHz would correspond to a magnetic field strength of 875 G.

$$\omega_{ce} = \omega_{rf} \tag{2.2}$$

When the frequencies coincide, the electrons are heated, absorbing the microwave power allowing the electrons to attain high energies making them ideal for ionization of an injected neutral gas. Electrons rotate around field lines in a right-hand manner as illustrated in Figure 5. When the electrons are in phase with the impinging microwaves, the electrons see a continual steady electric field over multiple rotations. This results in the efficient heating of electrons. In order for the continuous heating throughout the entire orbit of the electron to take place the impinging wave must be a right hand circularly polarized (RHCP) wave.

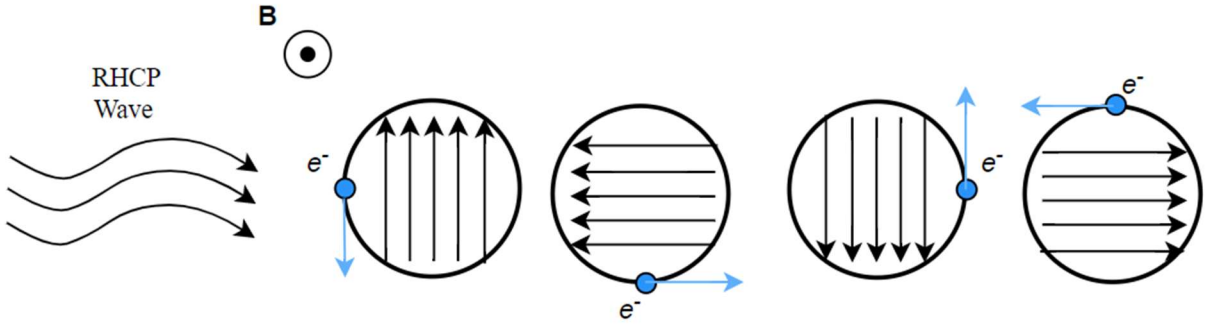

Figure 5: Electron rotating around a magnetic field line while being heated by a RHCP wave through ECR.

The heating of electrons in a non-uniform magnetic field occurs over a finite region as the field is consistently changing. Over the majority of an electron's path $\omega_{ce} \neq \omega_{rf}$ in this region the energy of the electron oscillates for the electron cyclotron frequency is not in phase with the electromagnetic wave frequency. The change of an electron's energy as it moves through an ECR region is shown in Figure 6.

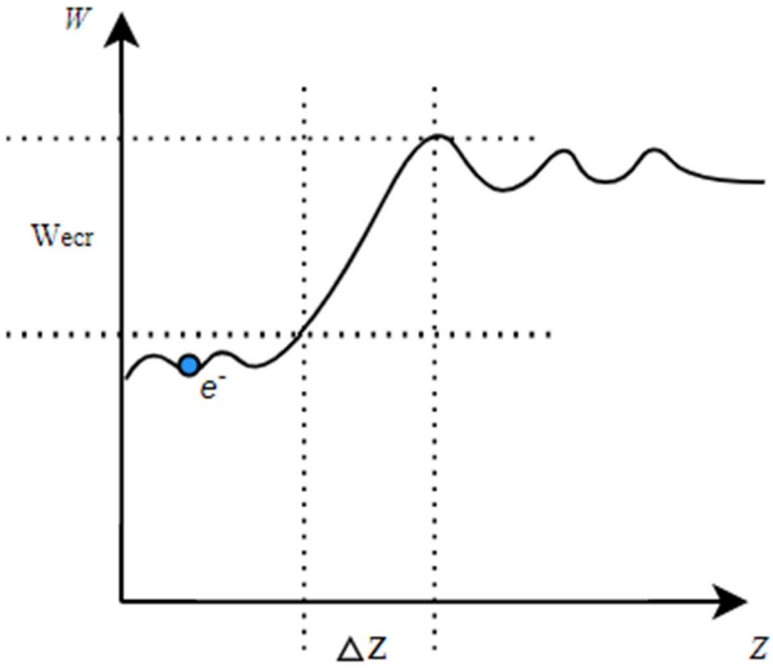

Figure 6: Energy gain and oscillation of an electron as it passes through a non-uniform magnetic field and ECR region.

Where Δz_{res} is the thickness of the resonance region expressed by equation (2.3) and is the region of the greatest energy gain by an electron. The average energy gained by an electron, W, as it passes an ECR layer is shown by equation (2.4) where v is the parallel velocity of electrons as they pass through the ECR region a E is the magnitude of the electric field. The average energy gained by an electron must exceed the ionization potential for ionization to occur.

$$\Delta z_{erc} = \left(\frac{2\pi v}{\omega|\alpha|}\right)^{1/2} \tag{2.3}$$

$$W = \frac{\pi e^2 E^2}{m_e \omega |\alpha| v} \tag{2.4}$$

$$\alpha = \frac{1}{B_{res}} \left(\frac{dB}{dz}\right)_{res} \tag{2.5}$$

Observing the above equations, the energy gained by an electron can be optimized. First, equation (2.5) α, is proportional to the magnetic field gradient and by creating a gradient that is low near the resonance zone the residence time of an electron inside the ECR region is increased. Second, improving the coupling of microwaves into the plasma cavity. To understand how waves propagate through a plasma a relationship between the frequency ω and wave number k known as the dispersion relation is helpful and is shown by equation (2.6). This relation describes when waves will and will not propagate through a plasma where μ_0 is magnetic permeability of free space and ε_0 is the electric permittivity of free space.

$$k^2 E + \omega^2 \mu_0 \varepsilon_0 E = 0 \tag{2.6}$$

In wave driven thrusters such as ECR thrusters, electromagnetic waves propagate in the direction parallel to the magnetic field. Only one type of wave is of great importance in ECR thrusters, right-hand polarized waves. Its dispersion relation tells when this wave will propagate and when it will be cutoff. The operation of ECR sources relies on the absorption and propagation of microwaves through a magnetized plasma [6]. For the propagation of waves in a cold plasma aligned with the magnetic field the dispersion relation can be separated into a right-hand polarized mode *R* and left-hand polarized mode *L*.

$$n^2 = R = 1 + \frac{f_{pe}^2}{f^2} / \left[\frac{f_{ce} k_{||}}{fk} - 1\right] \tag{2.7}$$

$$n^2 = L = 1 - \frac{f_{pe}^2}{f^2} / [\frac{f_{ce} k_{||}}{fk} + 1] \tag{2.8}$$

Each mode is equivalent to n^2, the index of refraction of the wave where $n = \frac{ck}{\omega}$, c is the speed of light and ω is the frequency. At the electron cyclotron frequency, the right-hand polarized mode has a resonance where the power is effectively coupled to the electrons making it the preferred mode for an ECR source [6]. The RHCP mode occurs where the ECR condition can be satisfied for $\frac{f_{ce}}{f} = 1$, resulting in $n \to \infty$ and the resonant absorption of microwaves. The left-hand polarized mode is cutoff and does not exist in the region of interest and will not have a strong interaction with the electrons [6]. Only RHCP waves are considered in the production of a ECR plasma.

2.3 Magnetic Nozzle

A magnetic nozzle is a magnetic field configuration used to convert the thermal energy of a plasma into directed kinetic energy producing thrust. A comparison can be drawn to the De Laval nozzle used in chemical propulsion. In a conventional nozzle, energy is converted from thermal energy to kinetic energy through the convergent-divergent geometry of the nozzle allowing the heated gas to expand supersonically. Through conservation of momentum the heated gas pushes against the walls of the nozzles as it exits producing thrust. In a magnetic nozzle, the momentum from the accelerated plasma is transferred to the magnetic circuit [7]. A magnetic nozzle consists of a diverging magnetic field topology of half a magnetic mirror created by either permanent or electromagnets. Charged particles within the magnetic nozzle become trapped on the field lines if efficiently magnetized allowing their acceleration along the diverging section of the nozzle.

Magnetic nozzles offer distinct benefits when compared to a physical nozzle. The most significant being the contactless handling of the plasma through the magnetic shielding of the

device reducing erosion leading to longer lifetimes and increased efficiencies. Magnetic nozzles are also highly adaptable when electromagnets are employed. The magnetic field topology can be changed in flight allowing different operational modes, such as high I_{sp} and low thrust or high thrust and low I_{sp}. Thrust vectoring is facilitated by the adaptability of a magnetic nozzle. Additionally, a magnetic nozzle is highly scalable. The operating principles of magnetic nozzles allow the scalability with power, size, and mass flow rate covering numerous uses [8].

The physics of plasma flow within a magnetic nozzle is complex and requires extensive study. The basic operation of a magnetic nozzle is as follows. A magnetic field formed by either permanent magnets or electromagnets generates a converging diverging magnetic field configuration. A plasma can be created in the upstream portion of the magnetic nozzle where the field is strong enough to fully magnetize the charged particles. The electrons can be magnetized at a much lower field strength than the ions. If only the electrons are magnetized, they are now attached to the field lines and follow the expanding magnetic field geometry, while ions can move freely. Plasma expansion initially occurs as a result of an existing electron pressure gradient and magnetic thrust. As electrons expand out, a space charge separation occurs between the electrons and ions possibly forming an electric field. This field allows the axial acceleration of ions downstream while also confining electrons upstream. Only a small portion of the higher energy electrons can make the potential jump following the ion beam [9]. The end result is the transfer of internal energy into thrust. The basic operation of a magnetic nozzle can be seen below in Figure

7. It is important to note magnetic forces do not exert work or supply energy to the plasma but enable the transformation of energy from one form to another.

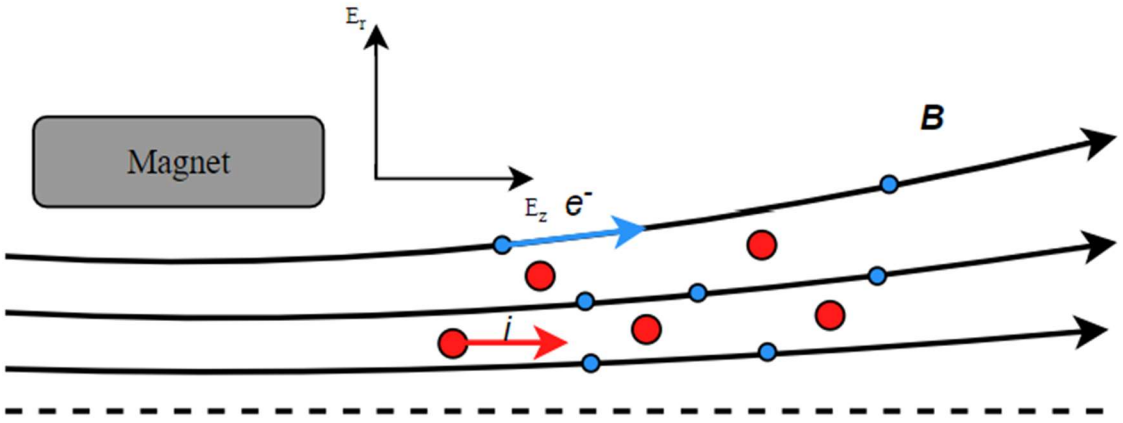

Figure 7: Basic operation and expansion of a plasma within a magnetic nozzle for use in electric propulsion.

The transfer of energy is driven by the magnetic thrust F_m and is described by equation (2.9).

$$F_m = -\mu \nabla_{||} B \tag{2.9}$$

$$\mu = IA = \frac{mv_{\perp}^2}{2B} \tag{2.10}$$

where μ is the magnetic moment and is invariant [2]. Therefore, μ must remain constant. Looking at equation (2.10), as the magnetic field deceases the perpendicular velocity $v_{\perp}$ must also decrease in order for μ to remain constant. The total kinetic energy described by equation (2.11) gives insight into the exchange of energy occurring within the magnetic nozzle. The magnetic field can only act as a mechanism for converting energy from one form to another.

$$K_{total} = K_{\perp} + K_{||} = \frac{mv_{\perp}^2}{2} + \frac{mv_{||}^2}{2} = constant \tag{2.11}$$

From equation (2.10) and (2.11) the parallel velocity of an electron, $v_{||}$, can be found with

$$v_{||} = \sqrt{v_{total}^2 - 2\mu B/m} \tag{2.12}$$

The above equation describes the motion of a particle as it traverses between regions of high magnetic field strength to low field strength. In order for the magnetic moment to remain constant as the particle sees an increasing magnetic field, $v_{||}$ must decrease and vice versa [2,10]. It is this parallel force resulting from the interaction of the magnetic moment created from the cyclotron motion of the particle and applied magnetic field which leads to the force seen in equation (2.9).

2.4 Plasma Acceleration and Detachment

Briefly mentioned in the previous section, the acceleration of the plasma is driven by an electric field, either in the form of an ambipolar electric field or double layers. An ambipolar electric field is an electric field where the length scales are on the order of the characteristic length of the device under test. While the length scale of a double layer is on the order of the Debye length. These fields form because of the higher mobility of electrons compared to ions. As a result of electrons being more mobile, an electron pressure gradient is established. The pressure gradient is formed ahead of the less mobile ions causing the electrons to flow downstream creating a space charge separation where the electron thermal energy is converted to directed longitudinal kinetic energy. The electric field created between the electrons and ions forms in order to maintain the quasi-neutrality of the plasma.

In order to produce thrust the plasma must detach from the field lines. The electrons inside of the thruster can be divided into three different populations. Free electrons, trapped electrons, and confined electrons. Electrons which have enough energy to detach from the magnetic nozzle field are termed free electrons. Trapped electrons are those that bounce back and forth at some point downstream in the magnetic nozzle and can possibly cause collisional ionization. Similar to

trapped electrons are reflected electrons that do not have enough energy to pass the potential barrier and are reflected back into the thruster. However, reflected electrons may pass through the ECR region a second time gaining enough energy to detach [11]. If the plasma does not detach, thrust will not be generated and the spacecraft will negatively charge.

Three classes of plasma detachment exist: collisional, collisionless, and magnetic reconnection detachment [10]. Each class offers a distinct possible method for how plasma is detached from the field of a magnetic nozzle. Collisional detachment is achieved through collisional effects of the particles within the plasma forcing the plasma to become detached. Collisionless detachment involves the detachment through the demagnetization of the charged species without the need for collisional phenomena. Lastly, magnetic reconnection is the detachment through the creation of an entirely new magnetic field configuration. The following discusses the individual methods of each class of detachment which could possibly achieve plasma detachment.

Collisional detachment can be accomplished through either resistive diffusion or recombination. Detachment through resistive diffusion occurs through cross field diffusion in the plasma resulting from the collision of particles within the field. The measure of cross field diffusion occurring in a magnetic nozzle can be determined by the magnetic Reynolds number $Re_m = UL/\eta$. Where U is the velocity, L is the length, and η is the magnetic diffusivity. A high $Re_m > 1000$ is needed to confine the plasma but intermediate to low values $1 < Re_m < 1000$ is required for detachment to occur [10]. Therefore, resistive detachment possesses conflicting requirements for the successful operation of a magnetic nozzle. The second method by which collisional detachment could possibly occur is by magnetic recombination. Recombination detachment occurs by the creation of neutral particles through the recombination of charged species. After the charge

particles have recombined, they are free to travel unaffected by the magnetic nozzle field. The base requirement of this method is a high electron collision frequency ν_{ei}, otherwise this method has little influence on plasma detachment [9,10].

The second class of plasma detachment is collisionless detachment and possibly occurs through loss of adiabaticity, inertia detachment, and induced field detachment. Loss of adiabaticity is a detachment mechanism where the plasma becomes detached by becoming demagnetized. This method requires not only one but both species to become demagnetized. Demagnetization of a single species is known as inertial detachment and is the second method of collisionless detachment. Here when a single species detaches from the magnetic field an electric field is established allowing neutrality to be maintained. Inertial detachment ensues when a system of particles possesses enough inertia to overcome the present magnetic forces [10,12]. The last method for collisionless detachment is induced field detachment. Detachment through this method is achieved by magnetic field stretching or by canceling out the applied fields, leading the plasma to become demagnetized. Magnetic field stretching occurs when the plasma kinetic energy exceeds that of the magnetic energy. The high energy plasma pulls the magnetic field as it expands deforming and stretching it. This results in the magnetic field lines being dragged to infinity where the plasma essentially does not have to detach from the field [9,10,12,13].

The final possible class of plasma detachment is magnetic reconnection detachment. Magnetic reconnection can be described as the processes leading to the breaking and reconnecting of oppositely directed field lines in a plasma resulting in magnetic field energy being converted to kinetic and thermal energy. This phenomenon has been observed in a variety of circumstances including Tokamak fusion reactors and celestial objects. The breaking and reconnecting of field lines is caused by the diffusion of plasma across the field lines leading to a new lower energy field

configuration that was previously not possible [10]. The basic process by which magnetic reconnection may occur is as follows. An initial field consisting of two magnetic field lines has some finite amount of cross field plasma diffusion. This diffusion leads to the subsequent tearing of the magnetic field lines creating a new lower energy configuration. The new lower energy configuration is dependent on the strength and direction of the induced field which is created by the induced currents. The new configuration can either be diamagnetic or paramagnetic. Diamagnetic fields are especially interesting because the interaction between the applied and induced field currents leads to a repulsive force producing thrust [10]. It is important to note that it may not be a single method which leads to the detachment of the plasma but a combination of all possible methods. Plasma detachment is complex but important for understanding the operation of magnetic nozzle thrusters. One of the primary features of ECR thrusters is the magnetic nozzle and it is important to have a basic understanding of the mechanisms in magnetic nozzles to ensure the efficient design and operation of the thruster.

CHAPTER 3

ECR THRUSTER DESIGN

3.1 Design Overview

In the previous chapter the physics underlying the generation and acceleration of a plasma in an ECR thruster was discussed. With an understanding of the physics behind the operation of the thruster, design choices can be made based upon these principles. The ECR thruster designed at Western Michigan University is based on the coaxial ECR thruster developed at ONERA [5]. The Western Electron Cyclotron Resonance (WECR) thruster is intended to be a small-scale low power thruster which can be studied at the university level. ECR thrusters are simple devices consisting of relatively few components. The external structure makes up the discharge chamber, front casing, and back casings. While the internal components consist of the microwave antenna, permanent magnet(s), and ceramic backplate. The dimensions of the WECR thruster are listed in Table 1 below. The inner conductor making up the antenna consists of a variety of different configurations all with a diameter of 0.08” (2 mm). These components are labeled in the CAD model displayed in Figure 8 below.

Table 1: WECR thruster dimensions.

WECR Thruster Feature	Dimension
Source chamber length	0.9” (22.86 mm)
Source chamber diameter	1” (25.4 mm)
Antenna diameter	0.078” (2 mm)
Front & back casing diameter	3” (76.2 mm)
Magnet casing diameter	2” (50.8 mm)

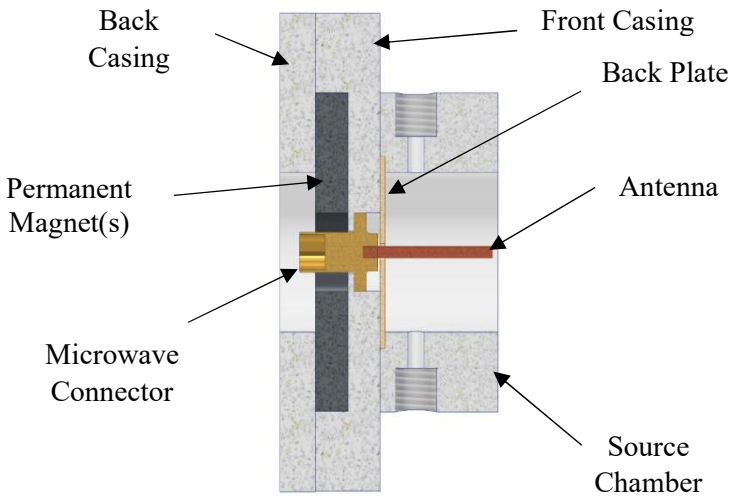

Figure 8: WECR thruster base design CAD model 1" source chamber diameter, 0.9" source chamber length, and 0.078" inner conductor diameter.

The external structure was fabricated from Aluminum 6061 while the antenna configuration consists of 110 copper attached to a Sub-Miniature Version A (SMA) connector placed in the radial center. Neodymium ring magnets are used to form the magnetic field creating the magnetic nozzle. To separate the more sensitive internal components from the plasma formed in the source chamber a ceramic back plate made of alumina is located in front of the microwave connector surrounding the antenna. As stated, the thruster operates on the ECR principle. The resonance region is created within the thruster cavity by microwave power being introduced at 2.45 GHz and a diverging magnetic field established by the permanent magnets. The fully assembled WECR thruster can be seen in Figure 9 mounted for testing.

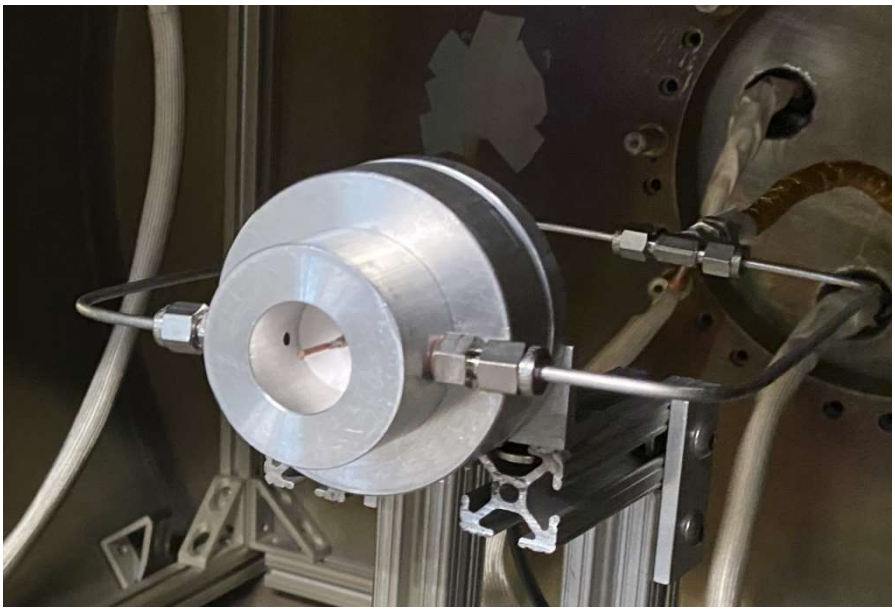

Figure 9: Assembled WECR thruster in vacuum chamber for testing.

The permanent magnets form the fields necessary for both the ECR region and the magnetic nozzle where plasma expansion occurs. In an attempt to optimize the thruster design, focus is placed on antenna geometry and magnetic field configuration. The intention is to improve upon microwave plasma coupling and overall thruster efficiency through changes in the above-mentioned design features. In order to achieve an efficient design, multiphysics simulations along with previous research conducted into small scale ECR thrusters was used to validate all design decisions. Initial two-dimensional COMSOL simulations were used as a starting point to test variations of antenna geometry and magnetic field configurations. The following sections cover the design of each major component or feature of the thruster including external structure, antenna geometry, gas injection method, magnetic field configuration, and the ECR source region.

3.2 External Structure

The external structure consists of three components: the source chamber, front casing, and back casing. The dimensions of the external structure and source chamber were chosen based on its small-scale design and previous work completed by researchers at ONERA [14, 15]. These

investigations showed the effect of altering geometry on the performance of the thruster. In the first study, Cannat et al. [14] created an analytic model and compared the output to experimental results for two different source chamber internal diameters of 13 mm and 27 mm. This study showed a larger diameter source chamber would result in an increase in ion beam current at the same flow rate, while at a lower power. Additionally, the pressure inside the thruster has significant impact on electron temperature. A thruster configuration with a larger source diameter will have a lower pressure in the source chamber, and therefore lower neutral density. A lower neutral density results in a decreased collision rate and leads to an increase in electron temperature which is favorable for thruster performance. With this in mind a source diameter of 1" (25.4 mm) was chosen for the WECR thruster. While an even larger diameter may have further increased the performance of the thruster, the WECR thruster is a small-scale design. The thruster design is considered small scale for its dimensions are less than the wavelength which it operates. For the case of the WECR thruster operating at 2.45 GHz this is under 4.8" (12.2 cm).

In a second study, Vialis et al [15] investigated geometric changes to both the internal and external structure of a 27.5 mm diameter ECR thruster. It was shown that I_{sp} increased with increasing length of the source chamber. The results from this study are illustrated in Figure 10, where three source chamber lengths 10 mm, 15 mm, and 20 mm were tested. The effect of varying the ratio of flow rate to microwave power on I_{sp} is shown. At lower ratios of flow rate to input power, Q_m/P, a larger source length results in greater I_{sp}; however, as the ratio is increased, a smaller difference between the source lengths of 15 mm and 20 mm occurs. The lack of performance of the shorter chamber could be a consequence of a fraction of the propellant not being ionized before expanding out of the source chamber.

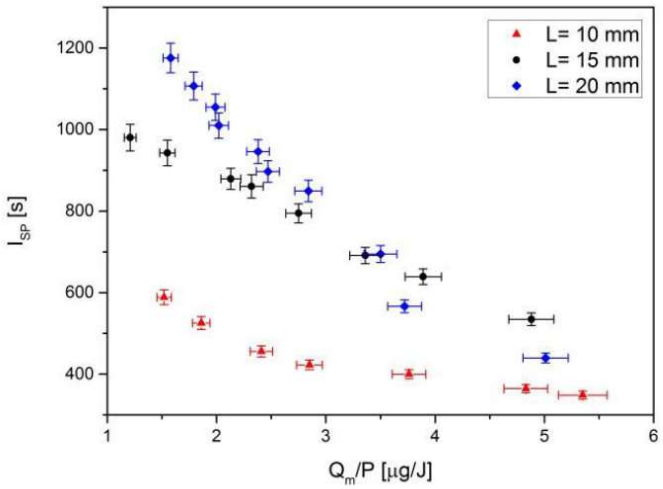

Figure 10: I_{sp} with changing Q_m/P for the three different source chamber lengths performed with an Inner conductor diameter = 1.7 mm and length =20 mm [15].

Additionally, a longer source length resulted in higher angular current density measurements, as shown in Figure 11 [15]. The longer source chamber led to an increase in neutral gas density and therefore a greater number of ionizing collisions. However, this also decreases the ion energy for increased pressure inside the source chamber. Increasing the source length has an advantage on total ion current, but a disadvantage for obtaining higher ion energies. However, a longer source produces the greatest I_{sp}, even though a drop in ion energy occurs. Taking this into account, a length of 0.9" (22.86) mm for the source chamber was chosen for the WECR thruster.

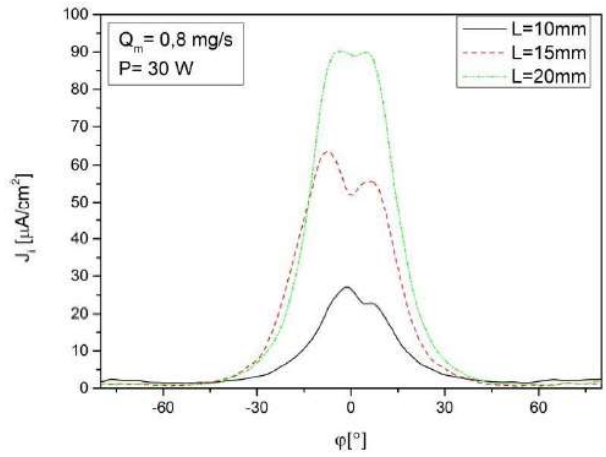

Figure 11: Ion current density measurements of three different source lengths at 0.8 mg/s and 30 W [15].

3.3 Antenna Design

The configuration of the antenna plays an important role in the coupling of microwaves to the plasma. Various antenna designs were investigated including straight rod, ring, and helical antenna. The first configuration, the straight rod is essentially a monopole antenna and will produce linearly polarized waves. This geometry has been used in all previous testing of coaxial ECR thrusters to date. The second configuration is a straight rod with the addition of a ring to the end. This design was used for a study in micro ECR ion thrusters and showed improved performance [16]. The performance of this design will be entirely different in the case of the ECR thruster because of a different magnetic field topology. The final configuration is a helical antenna. A helical antenna coiled in the correct direction will produce right hand polarized waves which is expected to most successfully heat the electrons. More care was put into this design for numerous factors effect its performance, including its crcumference, pitch, and aspect ratio of the antenna. These parameters where choosen caefully to allow the helical antena to perform optimally. The following equations are used to calculate pitch, α, impeadence, Z_0, and aspect ratio, AR, where S is the vertical spacing between coils, C is the circumference, λ is the wavelength, and N is the number of coil turns.

$$\alpha = tan^{-1}(\frac{S}{C}) \tag{3.1}$$

$$Z_0 = 140\frac{C}{\lambda} \tag{3.2}$$

$$AR = \frac{2N+1}{2N} \tag{3.3}$$

To note a quality antenna will be resonsant at the desired operating frequency matching the impeadence of the microwave circuit. This can be verified using a vector network analyzer (VNA). However, the impedance of antenna may be altered once the plasma has been ignited. Changing

the amount of transmitted and reflected power to the plasma. Each of the three confirguations is displayed in Figure 12.

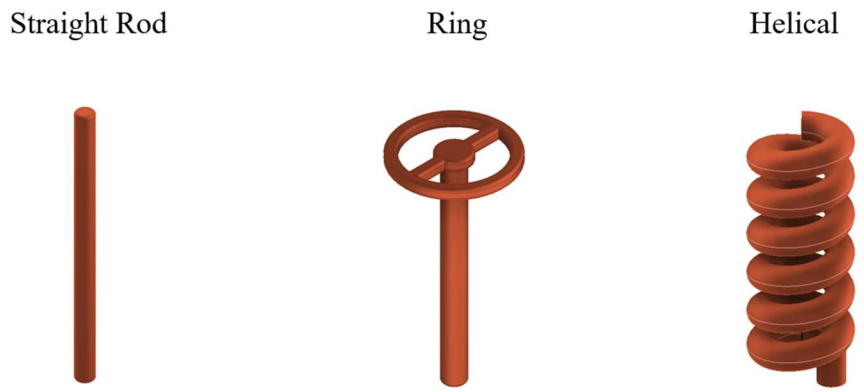

Figure 12: Microwave antenna design configurations.

As previously mentioned, the study conducted at ONERA on source chamber dimensions included an investigation into the internal geometry's effect on performance metrics. Shown below in Figure 13 is the effect from varying the length and diameter of an antenna [15]. The length of the antenna appears to have little influence on the performance of the thruster. While the antenna diameter has a more significant impact on thruster performance. A greater antenna surface area within the ECR region results in a greater potential to deposit power. This could possibly be the reason for the increased efficiency seen with increasing diameter. An increase in length of the antenna, however, will not affect power deposited into the ECR region; this may only result in losses due to a greater surface area. This is because the increased length of the antenna would not coincide with the ECR region.

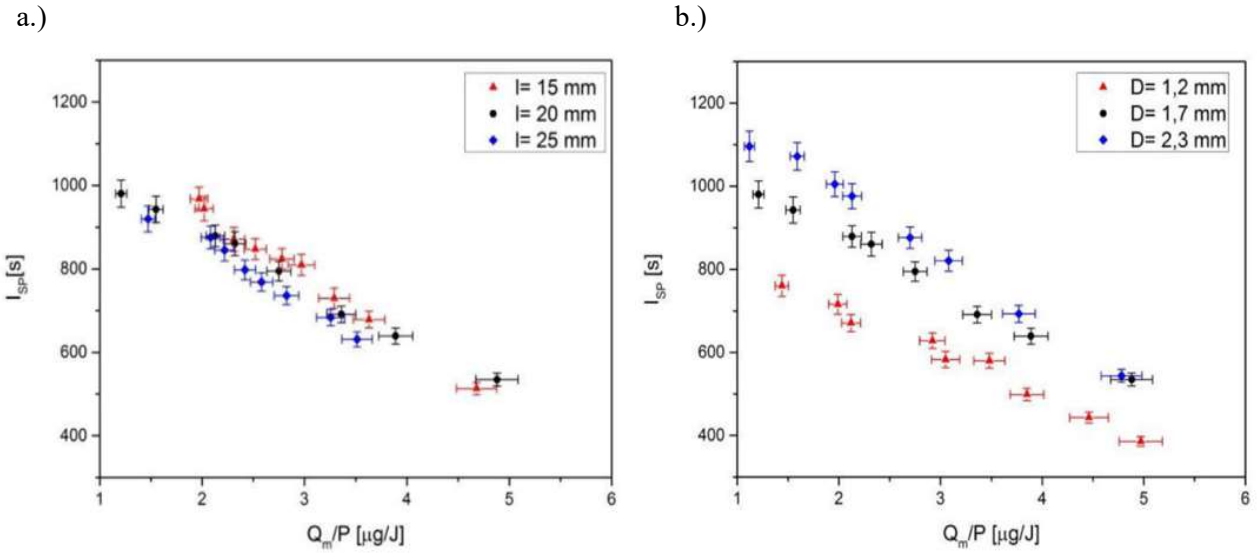

Figure 13: I_{sp} *of ECR thruster with variations in a.) antenna length showing decreasing* I_{sp} with increasing length *and b.) antenna diameter showing increasing* I_{sp} with increasing diameter *[15].*

The antennas used in the WECR thruster all possessed a conductor diameter of 0.04 in for effective microwave coupling. Each antenna did vary slightly in length, but as shown from Figure 13, length has little effect on the performance of the thruster. The length of the antenna configurations was determined by the need to make them resonant at a desired frequency. Each antenna configuration was analyzed with a nano VNA to confirm resonance at approximately 2.45 GHz. This allows for a greater impedance match between the microwave circuit and the antenna, reducing reflected power and improving microwave plasma coupling.

To investigate a design's effectiveness each antenna was simulated in the COMSOL RF module allowing a better understanding of the electric field patterns; these patterns are displayed in Figure 14. An antenna design method proposed by Koizumi and Kuninaka showed an effective design would produce numerous *E x B* points where the electric field lines are perpendicular to the magnetic field [16]. Knowing the energy gained by an electron as it passes through the ECR region from equation (2.4), it is important to coincide the regions of high electric field intensity with that of the location of the ECR region. The magnetic field in the case of an ECR thruster will possess

a greater axial component. Therefore, to create numerous $E\ x\ B$ points the electric field should be primarily radial. The below figure shows the effectiveness of an antenna to produce a primally radial field pattern.

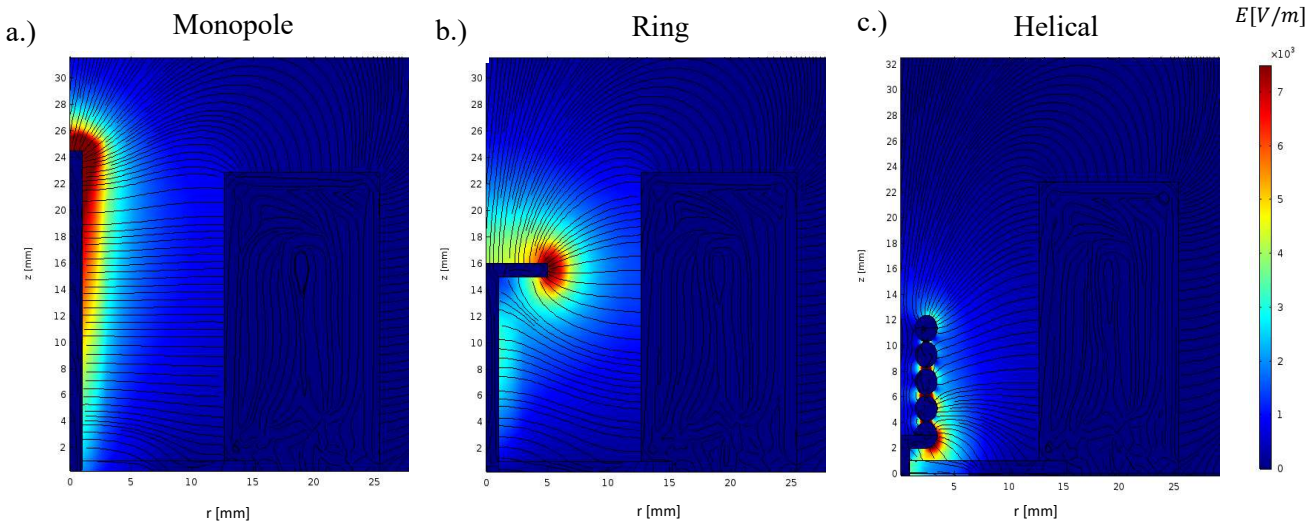

Figure 14:COMSOL RF antenna configuration simulations a.) straight rod, b.) ring, and c.) helical displaying electric field pattern.

The monopole antenna produces the most uniform field patterns with a significant amount of field lines perpendicular to the chamber walls and can be beneficial for electron heating. Looking at the ring antenna, the addition of the ring to the top of a monopole disrupts the monopole field patterns and leads to a large axial component. A strong intensity region is located at the edge of the ring; this could be optimal if this region is placed within the ECR region. Lastly, the helical antenna shows a similar pattern to the ring antenna but with a smaller axial component. The high field intensity regions of the helical antenna are located at the bottom turn and in between the individual coils. While the simulations do show the effectiveness of an antenna design based on its electric field intensity and pattern, they lack the capability of showing the effect of RHCP waves. These simulations were conducted in the presence of a vacuum and as stated the presence of a plasma can alter the performance of the antenna. However, the simulations give insight into

the electric field patterns formed by each design. Each of the above antenna configurations were used in the operation of the WECR thruster.

3.4 Gas Injection

The gas injection scheme plays an important role in the overall design of the thruster. In this section two propellant injection schemes will be considered, radial and axial injection, as shown in Figure 15. In the ECR thruster, plasma ignition occurs when sufficient free electrons gain energy from the ECR zone, enabling ionization via collisions. The thruster geometry is also very compact and must provide sufficient space for the gas injection, microwave power, and magnet configuration. Therefore, an injection scheme must provide numerous free electrons to the ECR region and enough available space for essential components.

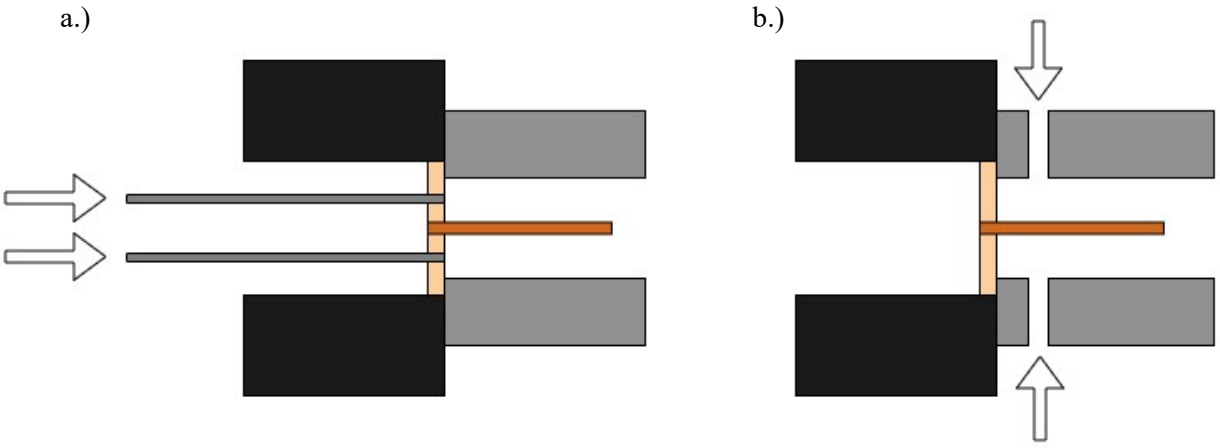

Figure 15: ECR thruster gas injection schemes a.) Radial gas injection and b.) axial gas injection.

Each method for gas injection possesses its own benefit. Radial gas injection allows added space in the rear of the thruster providing greater design freedom. Axial injection guarantees all neutral gas will pass through the ECR region but occupies design space. It has been shown that the best performance is obtained when gas injection is near the ECR zone. and the thruster would best perform when the ECR zone is farthest upstream near the backplate [18]. The WECR thruster

tested in this work utilized radial gas injection from two locations. The injection ports possess the same diameter as the inner diameter as the gas fittings used to facilitate neutral gas injection. Radial injection provides the simplest method for gas injection; however, the low number of injection ports resulted in a non-uniform gas distribution. While axial injection does provide the added benefit of utilizing the backplate. In axial injection gas is injected either behind or through the backplate. The backplate design then effects how the gas is distributed into the source chamber and can provide a more uniform gas distribution. This is done by cutting various patterns into the backplate and altering the distribution of the gas through patterns.

The ignition of the thruster can be a difficult process if the proper procedure is not followed. For the plasma to be ignited in the thruster discharge chamber a "puff" of gas must be injected. Nominal flow rates consisted of 1-2 SCCM of Xenon or 4-8 SCCM of Argon, but a much higher flow rate is needed to ignite the thruster. Ignition of the plasma is achieved through the use of a downstream valve labeled in Figure 16. This valve is closed allowing pressure to build up within the feed lines. This will temporarily increase the flow rate to high levels allow a large "puff" of gas to flow into the thruster source chamber. Initial experiments did not follow this procedure leading to failed attempts at igniting the thruster.

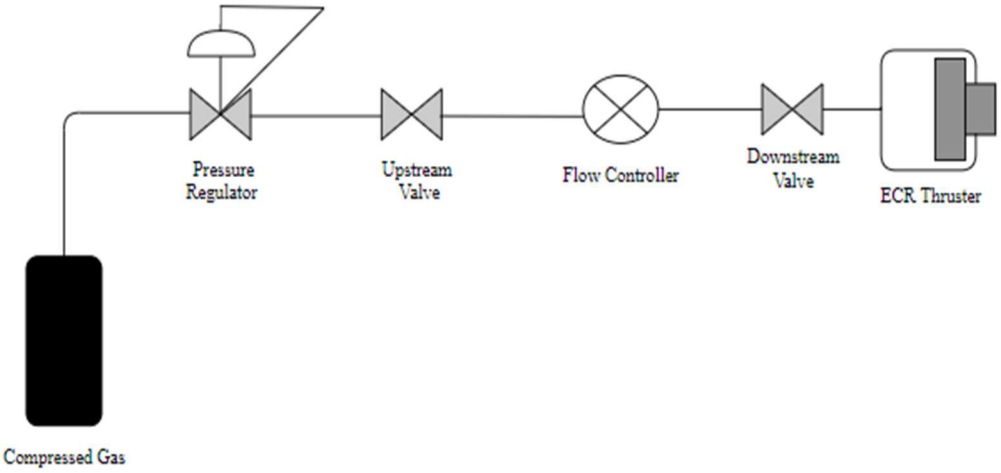

Figure 16: WECR thruster experimental gas flow setup.

3.5 Magnetic Field Structure

The magnetic field structure is one of the most import ant features of an ECR thruster. The field forms both the magnetic nozzle allowing the acceleration of the plasma and the ECR region which effectively generates the plasma. As discussed in the previous chapter magnetic nozzles are inherently complex and adding the requirement of plasma generation by ECR increases the design complexity. The magnetic field of the WECR thruster is formed by a set of strong neodymium permeant ring magnets. Each magnet possesses an outer diameter of 2" (50.8mm), an inner diameter of 0.5" (12.7mm), and a thickness of 0.25" (6.35 mm). The selection of permanent magnets over an electromagnet was based on the requirement of a single power source and the ability to change the position of the ECR zone by adjusting the axial position of the magnets. Future designs could provide the capability to either use an additional permanent magnet or an electromagnet allowing even more flexibility to study the effect of magnetic field topology on the thruster. It is important to note that no data were obtained with the use of a solenoid for the work completed in this thesis but is suggested for future experimental investigation.

The physics of magnetic nozzles are coupled and improving one feature may negatively impact another. Therefore, great care must be used in the design of the magnetic field topology of the thruster. The main functions of the magnetic nozzle in an ECR thruster are three-fold.

- Contain the plasma
- Accelerate and transfer momentum to produce thrust
- Aid in the generation of the plasma through ECR

First addressing plasma containment, radial wall losses are known to be a major loss mechanism in ECR thrusters [19]. Thus, to contain the plasma, a high magnetic field strength is preferred. It has been demonstrated that ions are accelerated to the walls by a radial electric field produced from a radial electron pressure gradient. Mitigation of the radial momentum flux to the wall was significantly reduced by increasing the field strength and is thought to be due to the change in the plasma profile and changes in the location of the ion acceleration [20, 21]. While increasing the magnetic field strength can accomplish the goal of preventing wall losses, this has a negative side effect on plasma detachment. An incredibly strong magnetic field makes it difficult for the plasma to detach from the field lines leading to the return of charged particles to the spacecraft/thruster and no net thrust. Inside the source chamber, it is preferred to have a strong magnetic field to preventing loss to the chamber walls; however, the opposite is preferred to aid in the detachment of the plasma. The tradeoff between plasma confinement and detachment is chosen based on satisfying the desired placement of the ECR region.

The WECR thruster was designed to operate at a frequency of 2.45 GHz which corresponds to an ECR magnetic field strength of 875 G. The position of the ECR region can be adjusted by moving the axial location of the permanent magnets within the thruster casings. This also alters the strength of the magnetic field within the source chamber. A study investigating the magnetic

field topologies in ECR thrusters by varying the axial position of the source chamber inside of an electromagnet was used for choosing the optimal position of the ECR region. The study showed an ECR condition satisfied near the backplate of the thruster leads to greater current density and ion energy compared to an axial position located slightly farther downstream [18]. In the design of the WECR thruster, space was made available to move the permanent magnets axially allowing the ECR region position to be changed. This allows for selection of the most optimal placement of the ECR zone, maximizing performance. The simulated magnetic field profile for the WECR thruster is shown in Figure 17 along with the corresponding ECR region. It is desired to possess the most axial field configuration, allowing the plasma to expand attached to the field lines out of the source chamber. In a permanent magnet configuration radial wall termination is difficult to remove. The field configuration below attempted to reduce radial wall termination to a minimum while still placing the ECR region in the desired location.

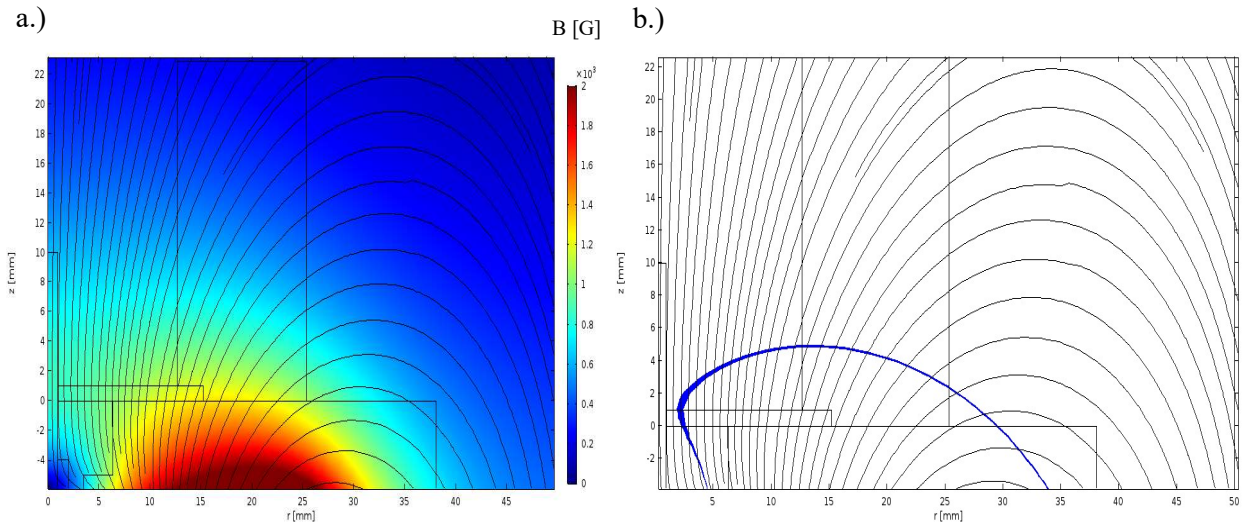

Figure 17: COMSOL simulation of a.) WECR thruster magnetic field configuration and b.) ECR region.

COMSOL simulations were used to verify the location of the ECR region when changes in magnet position, magnet inner diameter, and the number of magnets were made. To form the field displayed in Figure 17, two neodymium permanent magnets were placed in the thruster body

consecutively with a 10 mm space between the aluminum casing and the magnets. These figures display the magnetic field lines in addition to the contours, showing a magnetic nozzle structure with an axially decreasing magnetic field strength. This configuration allowed the ECR region to be placed both near the back plate and radial gas injection ports. A strong magnetic field exists within the chamber while the field strength drops off to a relatively low strength outside of the thruster. Measurements shown in Figure 18 were made by a Lakeshore gauss meter at various axial positions starting from the back plate to best capture the magnetic field gradient. These measurements show relatively good agreement with the COMSOL simulations with about a 2 mm difference in position of the ECR region. This difference most likely exists for the simulations excludes the radial magnetic field component. This magnetic field configuration was chosen for testing of the thruster since it possesses an adequate strength for plasma confinement and an ECR region in the desired location.

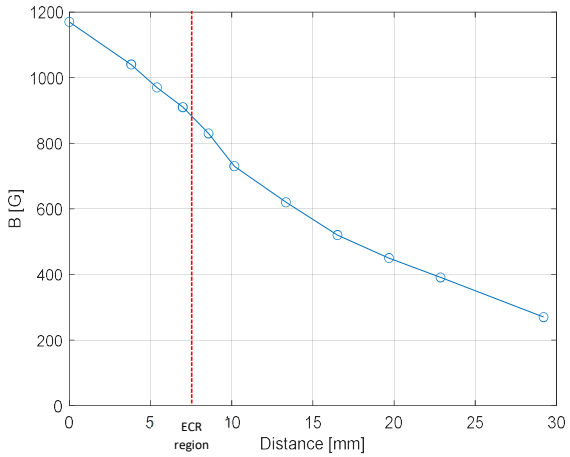

Figure 18: Axial magnetic field measurements starting from backplate of WECR thruster.

3.6 ECR Source Region

The primary principle of this thruster is ECR and to design the most effective thruster it is important to look at how to optimize the ECR region since it has significant impact on the overall

performance of the thruster. The WECR thruster will operate in the transverse electromagnetic mode, or TEM mode, in the coaxial line and the quasi-TEM mode in the source chamber [22]. TEM modes occur in coaxial lines where the electric and magnetic fields are transverse to the direction of wave propagation. It is important to note the electric and magnetic fields have regions of high field strength and low field strength based on the spatial pattern of the TEM mode. It is desired that the regions of high field strength coincide with the ECR coupling zones for the most optimal heating of the electrons [6].

As electrons pass through the ECR region, they are heated and gain gyro-kinetic energy, making them well suited for ionizing the gas. While ECR is only understood for single particle motion, this understanding can still be used to improve upon the performance of the thruster. The two primary methods for optimizing the absorption of energy in ECR sources of single particles are creating a low magnetic field gradient near the ECR region and improving coupling to the plasma. To achieve a small magnetic field gradient within the ECR region, manipulations to the magnetic field configuration can be made, including the addition of permanent magnets or electromagnets. By doing so the time spent by an electron in the resonance zone will increase and the energy imparted to the electron will be increased. The flexible design of the WECR thruster enables a variety of magnetic field configurations to be tested, allowing the possibility of a smaller gradient to be achieved. To find the desired field gradient, various sizes of permanent magnets were simulated. From the simulations the use of two neodymium permanent magnets each with the same dimensions a 2” OD, 1/2” ID, and 1/4” thickness would produce the smallest axial magnetic field gradient.

Several approaches were used to improve microwave plasma coupling. First, the antenna design method as discussed in section 3.3 was utilized to determine the effectiveness of antenna

designs coupled with different magnetic field configurations [16]. COMSOL simulations for each antenna were completed to show the effectiveness of each of the configurations. These simulations were effective at predicting whether increased performance would be possible with a selected antenna. An effective configuration creates numerous *E x B* points. The perpendicular electric field component created by the antenna along with the magnetic field gradient are used as the index of design. An effective antenna design places the higher intensity index regions within the ECR zone.

Figure 19 displays each of the antenna configurations and their effective heating regions along with the ECR region represented by the white region. The straight rod or monopole shows an effective heating region along its entire length. This results from there being a large perpendicular electric field component. The ring antenna does not have the same effective heating pattern along the length of the rod. The pattern was disrupted with the addition of the ring which changes the electric field, but it does allow for a higher intensity region to exist at a greater radial distance when compared to the straight rod. Finally, the helical antenna shows the worst overall performance. This is expected because of the lack of flat surfaces. While the helical antenna does show the worst expected performance from the standpoint of the antenna design method, this method does not account for the effect of RHCP waves effectively heating the electrons.

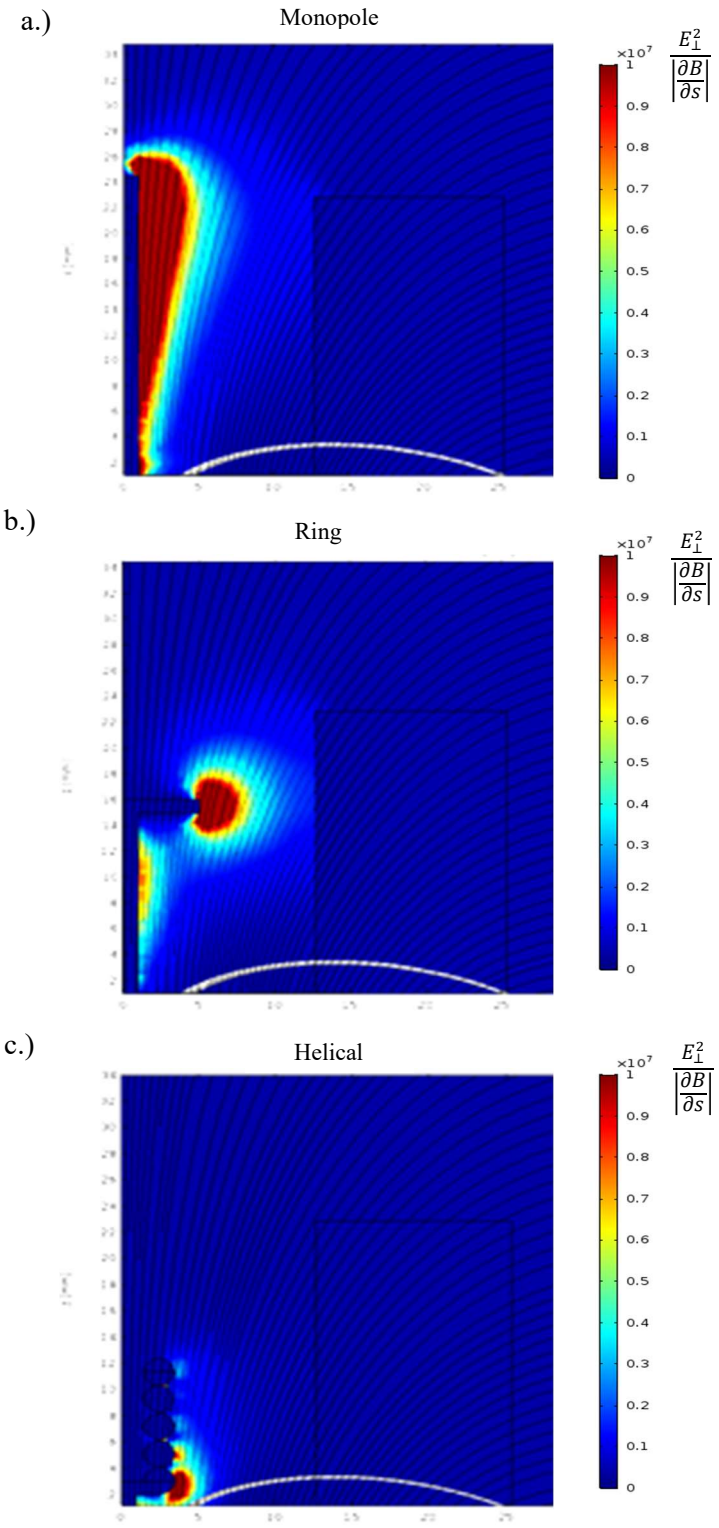

Figure 19: ECR effective heating regions and ECR region (white area) of a.) monopole, b.) ring, and c.) helical.

The simulations shown in Figure 19 were used as a baseline for determining the effectiveness of each possible antenna configuration. Compared to the simulations conducted by Koizumi and Kuninaka [16] for a micro ECR ion thruster the plots here appear to have similar trends with some designs have a smaller heating region while others a slightly larger region. Overall, this appears to be an effective method for determining antenna performance. An initial experimental investigation showed that the ring antenna was not effective at heating electrons due to difficulty in producing plasma and reflected power levels; therefore, it was excluded from further experimental characterization.

CHAPTER 4

EXPERIMENTAL SET UP

4.1 Facilities and Equipment

All testing was conducted at Western Michigan University in the Aerospace Laboratory for Plasma Experiments (ALPE). The following chapter provides an overview of the facilities, diagnostic equipment, and experimental setups used in the testing of the WECR thruster.

4.1.1 Vacuum Facility

Electric propulsion devices operate in the vacuum of space and to successfully test such devices on the ground a space like environment must be simulated. The WECR thruster was tested in a 1–m-diameter by 1.5–m-long cylindrical vacuum chamber at ALPE, as shown in Figure 20. This chamber utilizes a CTI-Cyrogenics on-board 250F cryogenic pumping system with a pumping capacity of 2,200 l/s of N_2 and can achieve a base pressure of 1E-7 Torr. Additionally, a Turbovac 1100C turbo pump is used during operation of the thruster to keep operational pressure to a reasonable level. All testing was completed at base pressures between 1E-6 – 7E-7 Torr with varying operational pressures determined by the operated flow rate, typically 1E-5 – 4E-5 Torr. At these pressures the mean free path, λ_{mfp}, is estimated to be between ~ 1 – 7 m. The mean free path is a measure of how far a particle will travel before a collision with another particle occurs and can be estimated by $\lambda_{mfp} = \frac{1}{\sqrt{2}n\sigma}$. Where n is the number density and σ is the total collisional cross section. Additionally, this parameter can be used to estimate how far a neutral particle will travel before an ionizing collision occurs [2]. Other important interactions include electron-neutral, ion-neutral, and charge exchange collisions. At the above pressures the mean free paths for electron-neutral collisions are on the order of a $1x10^2$ m. For ion-neutral and charge exchange collisions

the mean free path is much lower only around several meters. These values are estimated based on typical collisional cross sections at various energies in noble gases [4].

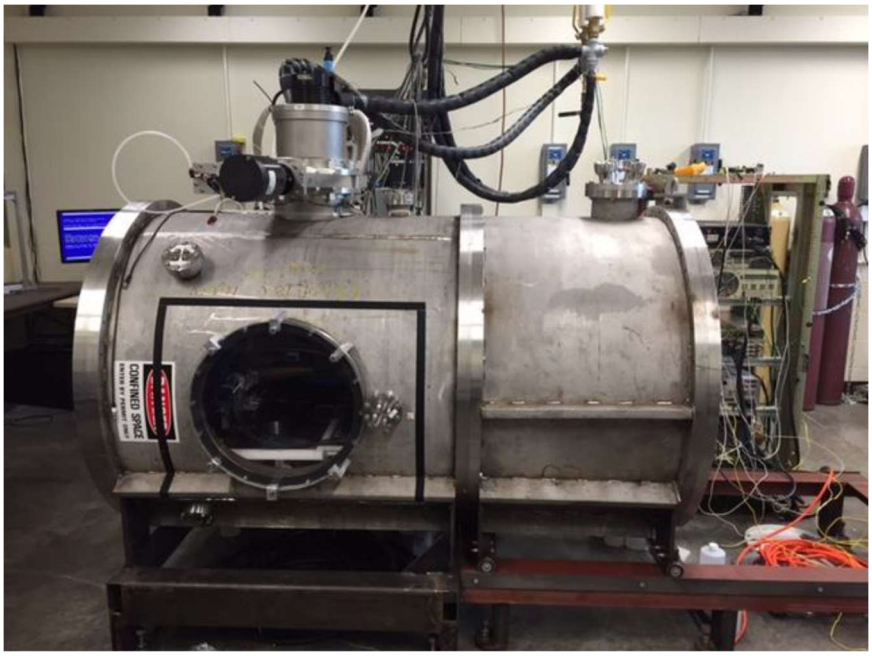

Figure 20: ALPE 1.5 x 1.0 m cylindrical vacuum chamber.

4.1.2 Gas Feed system

Neutral gas is injected into the thruster through the gas feed system illustrated in Figure 16. Compressed gas, typically Xenon or Argon is fed through a pressure regulator reducing the pressure to suitable levels and is then controlled by a Alicat flow control capable of 0 – 100 SCCM of flow. This allows the effective control of gas to the thruster at the desired flow rate. For the testing conducted in this work Xenon was utilized as the propellant at flow rates ranging between 0.5 SCCM to 2.0 SCCM. As discussed, it is important to be able to throttle the gas before it is fed into the thruster to allow for the successful ignition of the plasma. Once ignition takes place the flow rate to the thruster can be adjusted through the operation of the flow control.

4.1.3 Microwave System

The circuit diagram of the microwave power circuit is shown in Figure 21. The initial microwave signal is generated by a variable frequency oscillator at a constant frequency of 2.45 GHz. The signal is then amplified initially through a E-REON pre-amp with a saturated power output of 2 W. The signal is then sent to an E-REON PowerBlast 300 amplifier and boosted up to 300 W of power. A bi-directional coupler is introduced to enable the measurement of both the forward and reflected power. The power readings are displayed using a E4419B dual-channel power meter coupled with two HP 8484 A power sensors. A double stub tuner is introduced for microwave circuit matching to keep the power reflections to a minimum. Lastly, a DC block is used to float the thruster from the vacuum chamber. The circuit matching is done individually for each antenna design at the beginning of the testing phase. Effective power transmission through the circuit is essential for generating and sustaining the plasma at low power levels.

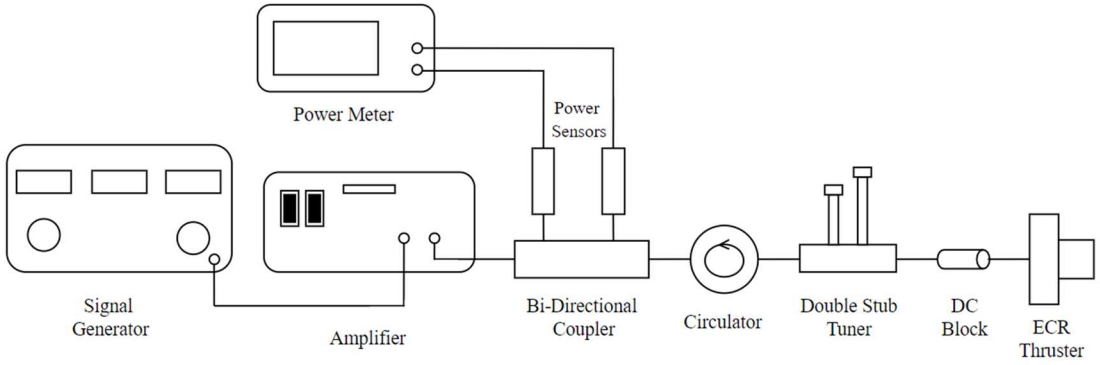

Figure 21: Microwave circuit diagram utilized in WECR thruster testing.

4.2 Plasma Diagnostics

Numerous techniques exist to probe the plume of an EP device, providing an effective way to collect data and gather information about the current, potential, temperature, density, energy, and particle velocity of a plasma. This information can give insight into the overall performance of the thruster. Here, a series of plasma diagnostic equipment is used to characterize the WECR

thruster including a Langmuir probe, Faraday cup (FC), and retarding potential analyzer (RPA). These diagnostic tools are described in the following sections.

4.2.1 Langmuir Probe

Langmuir probes provide a simple method for analyzing the state of the plasma properties in the plume of an EP device. A cylindrical Langmuir probe has been designed to obtain measurements of electron density, electron temperature, and plasma potential. Careful consideration must be used in the design and fabrication of the probe. All gaps between the probe tip and electrode must be eliminated for this can lead to excess collected current. Tungsten was used as the probe's center conductor while alumina was utilized as the insulator. The plasma density is expected to be on the order of ~1 x 10^{15} with expected electron temperatures ranging from 15 – 30 eV. The exposed portion of the probe consisted of a 1/8-in-diameter by 1-in-long tungsten wire. The probe was connected to a 2400 Keithley source meter having the capability of sourcing ±200 V while measuring up to 100mA.

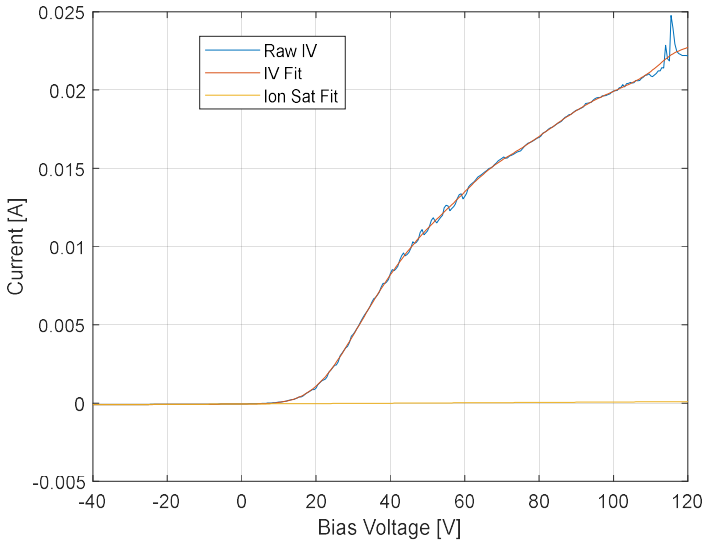

Figure 22:Example raw IV trace and fits of raw data from Langmuir probe.

To obtain an IV trace the probe is first biased to a large negative potential and when emersed in the plasma will attract ions and repel electrons. This region is considered the ion saturation region and is described by the equation below:

$$I_{i,sat} = -\exp(-1/2) e n_0 A_s \sqrt{\frac{eT_e}{M_i}} \tag{4.1}$$

where n_0 is the plasma density, A_s is the sheath area, T_e is the electron temperature, M_i is the ion mass, e is the elementary charge. The probe is then biased to a large positive potential where it will saturate and only collect electron current. The electron saturation current $I_{e,sat}$ can be estimated from equation (4.2) [23]:

$$I_{e,sat} \approx -323 \cdot I_{i,sat} \tag{4.2}$$

The result of this process will be a curve similar to the graph illustrated in Figure 22 where the IV trace and fits of the data are shown.

As the plasma created by the thruster is magnetized, the recommended orientation for a cylindrical probe when nonnegligible fields are exist is perpendicular to the magnetic field of the thruster for the most effective surface collection area [23]. The probe is placed at a distance of 175 mm from the exit of the thruster leading to a field strength of ~15 G while this is not significant the probe is still placed in the recommended orientation accounting for any effects. The plasma potential, V_p, is found by finding the second derivative of the electron current where V_p occurs at the maximum of the derivative. To determine plasma density and electron temperature the electron energy distribution function (EEDF), $F(\varepsilon)$, can be found through the Druyvesteyn method, which is preferred when measurements are made in a magnetized plasma. This method calculates the EEDF in the electron retarding region, where there is no electron sheath resulting in the dependence on the ratio of probe size to Deybye length to be removed [23]. The EEDF can be

found from equation (4.3) and is proportional to the second derivative of the electron current with respect to $\varepsilon = V_p - V_B$. Electron density and electron temperature can then be estimated from equations (4.4) and (4.5).

$$F(\varepsilon) = \frac{2}{e^2 A_s}(2m_e e\varepsilon)^{1/2}\frac{d^2 I_e}{d\varepsilon^2} \tag{4.3}$$

$$n_e = \int_0^\infty F(\varepsilon)d\epsilon \tag{4.4}$$

$$T_e = \frac{2}{3n_e}\int_0^\infty \varepsilon F(\varepsilon)d\epsilon \tag{4.5}$$

These properties give insight into the performance of the WECR thruster. The probe setup and orientation for initial testing of the thruster can be seen in Figure 23.

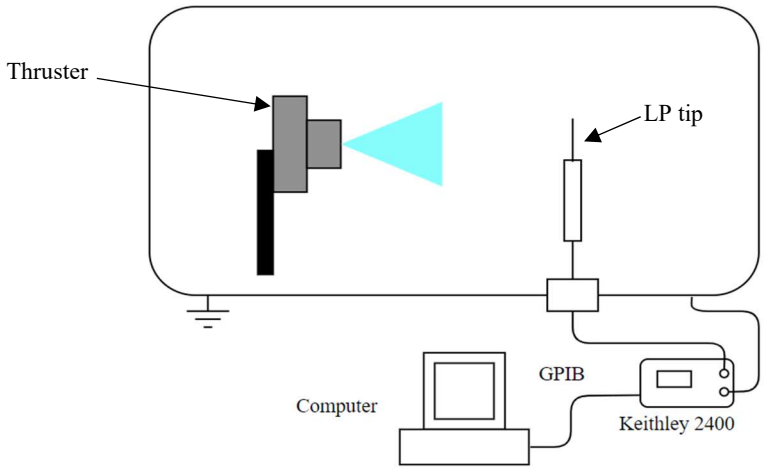

Figure 23: Langmuir probe experimental setup.

4.2.2 Faraday Cup

A Faraday cup (FC) is a diagnostic device used to measure the ion current in the plasma plume of an EP device. This is accomplished by biasing the collector of the cup to a negative potential, allowing for the collection of ions and repulsion of electrons. A diagram of the FC and its components used in the testing of the WECR thruster is illustrated in Figure 24. An FC, unlike

a planar probe, is not significantly affected by sheath expansion due to its particular geometry [24, 25]. FC consists of a hollow cylinder forming the cup, a collimator near the front of the probe with the capability of being utilized as a secondary electrode, and an external housing encompassing the internal components.

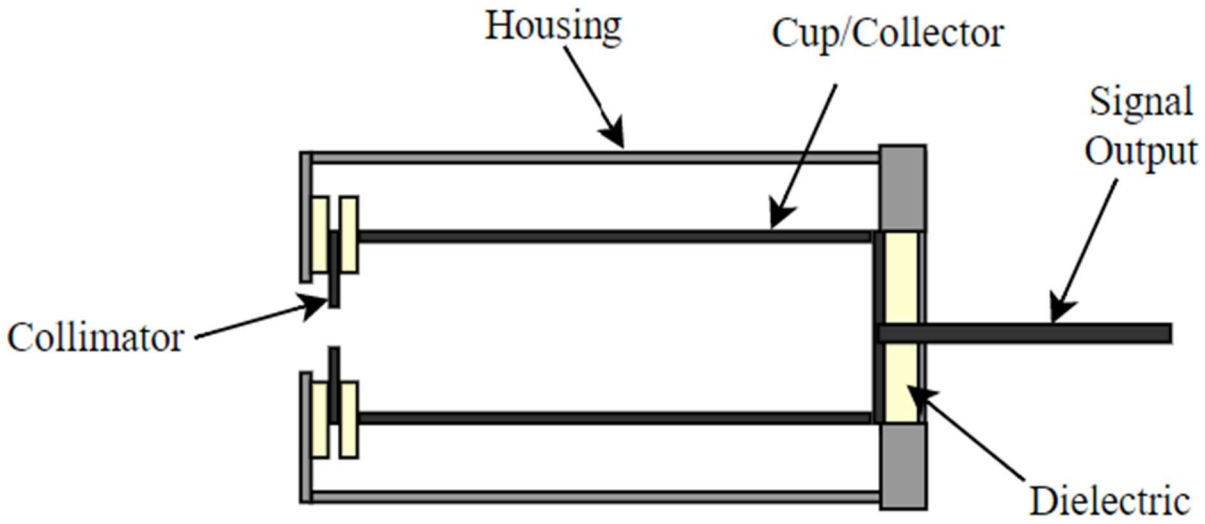

Figure 24: Faraday cup configuration.

The FC used in this work consists of a stainless-steel aperture with a ~0.2-in-diameter and that is left floating. It has been shown that the addition of a biased electrode placed between the collector and point of collimation to improve secondary electron emission (SEE) is not needed [24]. SEE is the emission of electrons from a metal surface and can lead to inaccurate current measurements. The cup itself made of aluminum 6061 with a 0.7-in-internal diameter and a 1/4-in-length. The length of the cup is the primary factor contributing to secondary electron emission recollection. The cup length is directly related to the number of secondary electrons being recollected by the cup walls [26]. During testing of the FC an applied cup bias is chosen by setting a potential that will result in no significant additional current gained by further increasing the bias. To complete the angular current density, scan the FC is mounted and placed on rotational motion stage. Current measurements are recorded by the Keithley 2400 while sourcing the constant cup

bias. The FC position is swept from -90° to 90° providing the angular current density distribution. Shown below in Figure 25 is the setup used in the testing of the WECR thruster to obtain the total ion current and mass utilization.

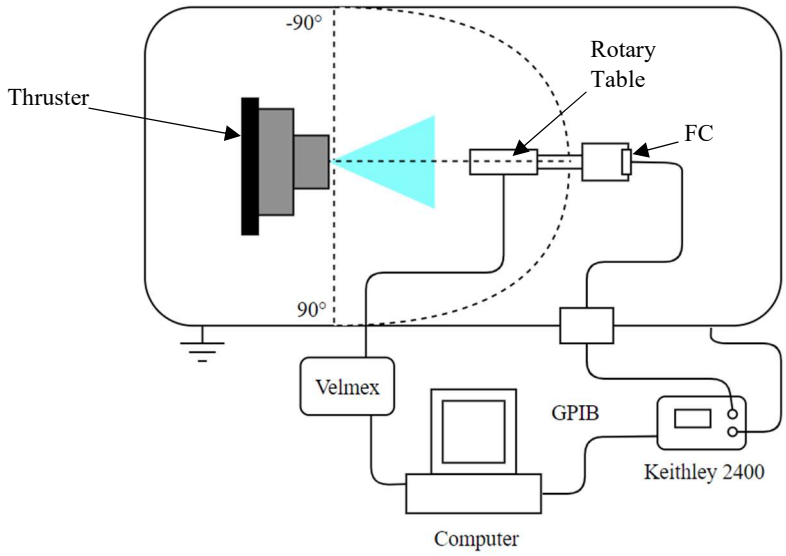

Figure 25: Faraday cup experimental setup.

Several thruster parameters can be determined from the FC measurements, with the addition of RPA measurements discussed in the following section, that provide significant insight into the overall performance of the thruster. The total ion current I_i shown in equation 4.6 can be directly determined from the angular ion current density distribution.

$$I_i = \int_{-\frac{\pi}{2}}^{\frac{\pi}{2}} J_i(\theta)\pi D^2 \sin(\theta) d\theta \tag{4.6}$$

$$T = \int_{-\frac{\pi}{2}}^{\frac{\pi}{2}} J_i(\theta)\frac{M_i}{e} v_i \pi D^2 \sin(\theta)\cos(\theta) d\theta \tag{4.7}$$

where $J_i(\theta)$ is the angular current density and D is the distance, the probe is from the exit plane of the thruster. Thrust T can also be estimated from the ion current density with the addition of the mean ion velocity v_i using equation 4.7. The mean ion velocity is found from the IEDF and will be obtained from RPA measurements. Additionally, metrics required to calculate thruster

efficiency, mass utilization, η_m, divergence factor, η_d, and energy efficiency, η_e, can be calculated from FC measurements, allowing the total efficiency η_T of the thruster to be estimated.

$$\eta_m = \frac{I_i M_i}{\dot{m}_g e} \tag{4.8}$$

$$\eta_D = \frac{T}{\dot{m} v_i} \tag{4.9}$$

$$\eta_e = \frac{I_i E_i}{P_{MW}} \tag{4.10}$$

$$\eta_T = \eta_e \, \eta_m \, \eta_D^2 \tag{4.11}$$

The I_{sp} can also be used as a performance parameter and can be found in terms of the effiecncy parameters.

$$I_{sp} = \frac{T}{\dot{m}_g g_0} = \frac{\eta_D \eta_m v_i}{g_0} \tag{4.12}$$

These metrics allow for the characterization of the WECR thruster.

4.2.3 Retarding Potential Analyzer

An RPA is a plasma diagnostic tool used for the analysis of the ion energy distribution in a plasma. This tool consists of a series of grids which are biased electrostatically to systematically repel the constituents of the plasma [27]. Located behind the biased grids is a collector that will measure current. RPA's can consist of three or four gird configurations with each grid positioned parallel to each other inside a housing. In both configurations the first grid is floating at the plasma potential to prevent the downstream grids from influencing the plasma. The second and if a fourth grid is used are biased negatively to act as electron repelling and suppression grids, respectively.

In either configuration the third grid is swept positively from 0 V to the desired positive potential. As the potential is increased less ion current can pass through the retarding grid forming a plot as shown in Figure 26. The blue trace represents the measured current for an increasing retarding grid bias, while the second trace represents the IEDF.

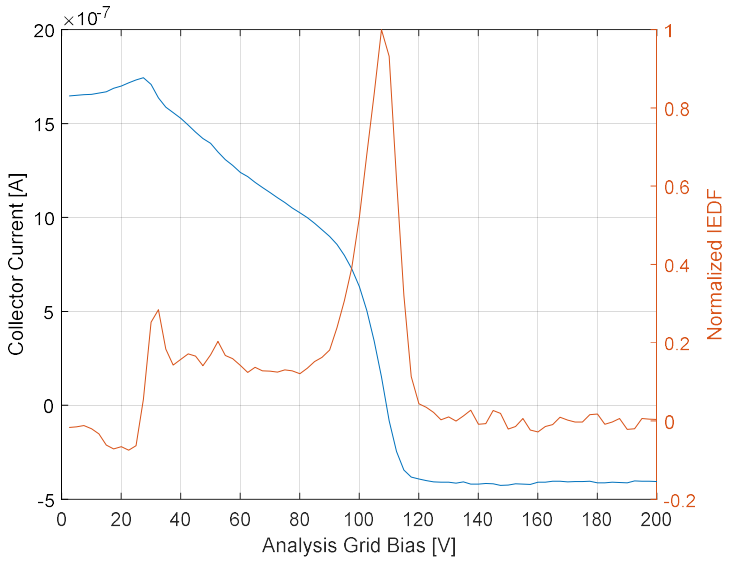

Figure 26: RPA collected current trace and derived ion energy distribution function.

Current is measured as a function of the retarding grid potential. An energy distribution function can be determined from this I-V curve by differentiating the collected ion current with respect to the bias of the retarding grid.

$$\frac{dI_{coll}}{dV_{bias}} = -f(E) \tag{4.13}$$

A four grid RPA was previously designed at ALPE for use in low power Hall thruster testing [28] and will be used for ion energy measurements of the WECR thruster. The RPA body, grids, retention rings, and wires are made from 316 stainless steel. All grid wires are insulated by alumina tubing. MACOR is used between the grids and between the grid stack and the RPA body to isolate everything. The repelling grid is biased to a negative potential sufficient to repel a

majority of the electron current within the plasma plume. The suppression grid is biased to -45V, this grid acts as a second electron repulsion grid. Preventing any additional electrons created within the RPA from providing a more accurate reading. The third grid is swept from 0 V up to 400 V to obtain $I_{coll}(V_b)$. The experimental set up is displayed in Figure 27.

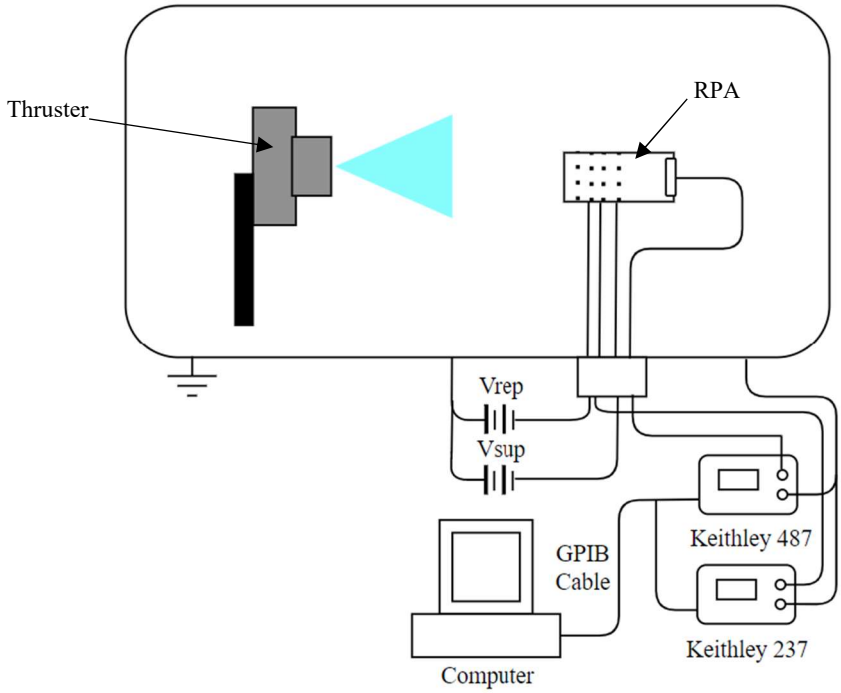

Figure 27: RPA experimental set up.

Data collected from RPA measurements allows the IEDF to be found where the mean ion energy can be extracted from the distribution. The remaining efficiency parameters mentioned in section 4.2.2 can be estimated with the addition of the mean ion energy, which in turn allows the thrust to be calculated. An effective characterization is possible with the completion of the above-mentioned plasma diagnostic experiments.

4.3 Instrumentation and Data Acquisition

To enable the experiments described in the previous section three separate Keithley measurement units were utilized, a Keithley 2400, 487, and 237. The Keithley 2400 is a highly stable DC source and a multimeter. This unit was used to bias the conducting probe for both the

Langmuir probe and FC testing. The Keithley 237 high voltage source measurement unit (SMU) and the 487 picoammeter were used only for RPA measurements. To sweep the retarding grid of the RPA, the Keithley 237 was applied concurrently with the Keithley 487 for precise current measurements. The combination of the above units allowed for the effective measurement of the data needed to characterize the thruster.

Data acquisition and experimental control was accomplished through the use of LabVIEW. Three separate LabVIEW VIs were used for each of the aforementioned experiments. These programs facilitated control of the diagnostic equipment and instrumentation. To interface with the Keithley 2400, 487, and 237 a GPIB-USB-HS+ cable was used to transmit collected data from the instrumentation to the LabVIEW computer allowing it to be recorded. Data obtained from all plasma diagnostic tests is processed through MATLAB. The processed data obtained is displayed in the following chapter.

CHAPTER 5

EXPERIMENTAL RESULTS

5.1 Experimental Overview

The experimental setups discussed in Chapter 4 were utilized to obtain results addressed in the following chapter. The WECR thruster demonstrated first light and continuous plasma using three different antenna configurations at power ranges between 30 - 100 W and flow rates ranging from 0.5 – 2 SCCM of xenon. Figure 28 displays the operation of the WECR thruster on xenon. The experiments provided data for the full performance and plume characterization of the WECR thruster. Additionally, these experiments provided further data for studies into ECR thrusters and were used to produce an optimized design.

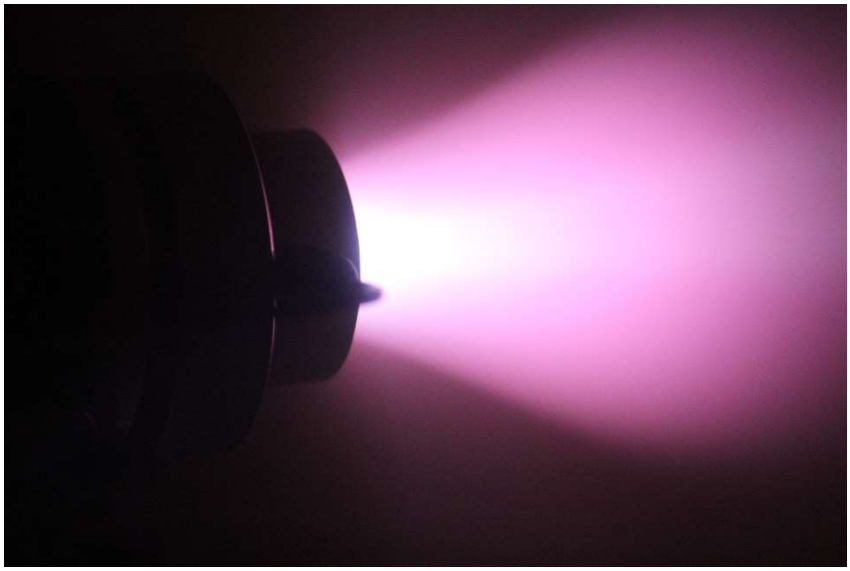

Figure 28: Operation of the WECR thruster during characterization at 1 SCCM and 20 W.

5.2 Plasma Diagnostic Probe Results

The following sections describe the results obtained from each plasma diagnostic test in detail.

5.2.1 Langmuir Probe

Time averaged current measurements as a function of applied voltage were performed with a LP in the plume of the WECR thruster to obtain the following plume properties: electron density, plasma potential, and electron temperature. As mentioned in section 4.2.1 the Druyvesteyn method enables a more effective estimation of the plume properties in a magnetized plasma. The Langmuir probe experiments of the WECR thruster were conducted for varying flow rate of xenon. Measurements were made 175 mm downstream of the thruster exit plane with the cylindrical Langmuir probe described in section 4.2.1. The objective of these measurements was to compare the plasma properties of a coaxial monopole and helical antenna, providing insight into whether a helical antenna could be more beneficial for microwave plasma coupling. Figure 29 shows the plume properties of both antenna configurations.

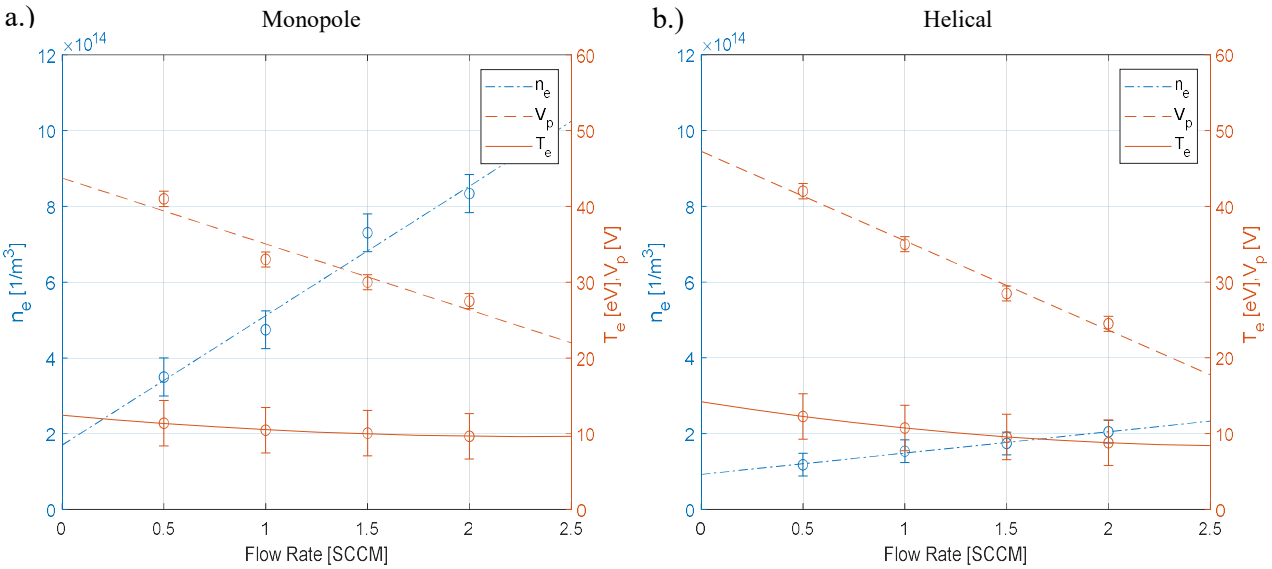

Figure 29: Langmuir probe plasma properties at 20 W absorbed power for changing flow rate a.) monopole antenna and b.) helical antenna.

The estimated plasma properties display expected trends with increasing flow rate. A maximum electron temperature of 11.4 eV is obtained for the monopole antenna at 0.5 SCCM. At the same flow rate the maximum obtained electron temperature for the helical antenna was 12.3 eV. Similarly at the lowest flow rate the maximum plasma potential is obtained for both the

monopole and helically antennas at 41 V and 42 V respectively. The greatest electron density was measured at the highest flow rate of 2 SCCM for both antennas with the monopole antenna reaching $8.34 \text{ x } 10^{14} \frac{1}{\text{m}^3}$ and the helical antenna measuring $2.05 \text{ x } 10^{14} \frac{1}{\text{m}^3}$.

Analyzing the trends observed and the possible mechanisms which resulted in the obtained Langmuir probe data. At flow rates above 1.5 SCCM the electron temperature T_e shows minimal dependence on flow rate. It was shown by Cannat et al. [14] at flow rates below 0.5 SCCM an exponential increase in electron temperature occurs. It is thought a similar trend would occur if measurements were made near 0.25 SCCM. This results at lower flowrates where electrons have additional time to gain energy before a collision, leading to an increase in electron temperatures. When analyzing the plasma potential, V_p, and electron density, n_e, there is an observable linear relationship with varying flow rate. The negative effect of increasing flow rate on plasma potential can be attributed to the drop in electron temperature [29, 30]. Where electron temperature and plasma potential are related through the polytropic coefficient or ratio of specific heat, γ_e, $\frac{\phi_{max}}{T_{e0}} = -\frac{\gamma_e}{\gamma_e - 1}$ [29]. Additionally, the plasma potential profile is thought to be highly dependent on the initial conditions in the source, for a higher pressure or flow rate alters the electron energy [31]. Evidently, operating at a lower flow rate is the most beneficial in terms of plasma potential and electron temperature. Ion energy is linked to electron energy, where a greater ion energy results in an increase in thrust [29]. Therefore, a greater electron energy would be beneficial. Furthermore, electron density is directly related to flow rate. When there is an increase in flow rate, there is an increase in electron density. This relationship is easily explained since there is more propellant to be ionized at higher flow rates, resulting in a greater collected current.

As shown in Figure 29 each antenna configuration exhibits similar trends, but the helical

antenna appears to lack in electron density production. The rate of change of the electron density with flow rate is significantly less in the helical antenna compared to the monopole antenna. This outcome may result from less efficient microwave plasma coupling than what was expected. Less efficient coupling can be observed from the level of reflected power throughout testing. The reflected power in the helical antenna fluctuated much more than that what was observed with the monopole antenna. The transmitted and reflected microwave power during testing is described in more detail in section 5.3.3. COMSOL simulations conducted with each antenna configuration agree with the results observed. A large perpendicular electric field component could not be created with the helical antenna, resulting in poorer performance compared with the monopole antenna.

Figure 30 shows a comparison of the electron temperatures obtained for varying flow rates for both the monopole and helical antennas. An objective of this work was to test the hypothesis that the helical antenna would result in a greater electron temperature, indicating that more energetic electrons are produced due to the fact that the helical antenna more effectively heats the electrons as it creates RHCP waves. Previous work has shown that greater thrust results from increased electron temperature in wave driven thrusters [14,19]. As a result of the increased electron temperature and presumably thrust, an improved performance with the helical antenna could be calculated. A ~13% uncertainty was calculated for electron temperature measurements utilizing standard error propagation methods detailed in reference [23]. Taking this error into account the slight increase measured in electron temperature with the helical antenna cannot be said to have produced a greater value than the monopole antenna, as observed from the figure below. Further investigation into the performance of the helical antenna will be discussed in the following sections showing that the helical antenna lacks in the production of total ion current and

high energy ions.

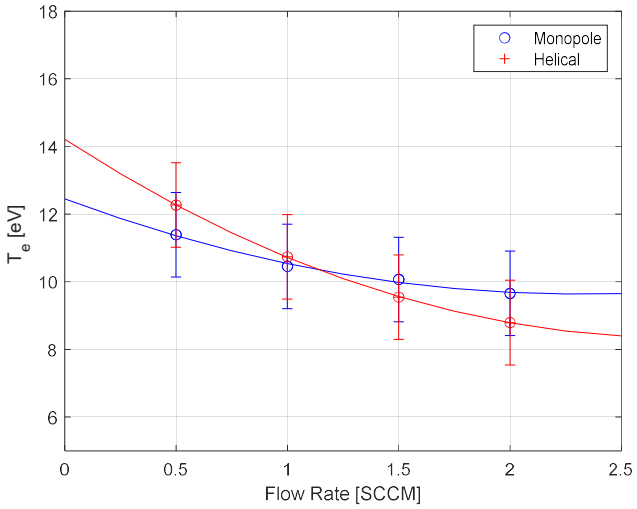

Figure 30: Electron temperature measurement comparison of monopole and helical antennas at 20 W for changing flow rate.

5.2.2 Faraday Cup

The FC experiments provided measurements that allowed for the estimation of total ion current and mass utilization. FC measurements were made ~11.5" (29.2cm) downstream of the thruster at various absorbed microwave powers and flow rates. The FC would transverse the entire angular profile of the thruster from -90° to 90° providing the angular ion current density profile. To note, measurements above 30 W with the helical antenna could not be accomplished due to fluctuations in the absorbed and reflected power causing irregular measurements.

From the angular sweep of the FC the following current density profiles in Figure 31 were found for the monopole antenna at various microwave absorbed powers for flow rates of 1.5, 1.0 SCCM, and 0.5 SCCM. Reflected power levels were typically measured or be under 5 W in all cases. For most power levels, the maximum current density occurs along the central axis of the thruster. Increasing the microwave power tends to raise the peak current density and cause the current density at the wings of the profile to increase. Similar profiles are found at all flow rates with the current density increasing with microwave power. The largest increase in current density

is observed when increasing microwave power from 10 W to 17 W, indicating a higher microwave power is required to initiate a reaction to generate a greater amount ion current. A maximum current density is achieved along the central axis at 40 W of absorbed power and 1.5 SCCM of ~ 41 μA/cm^2.

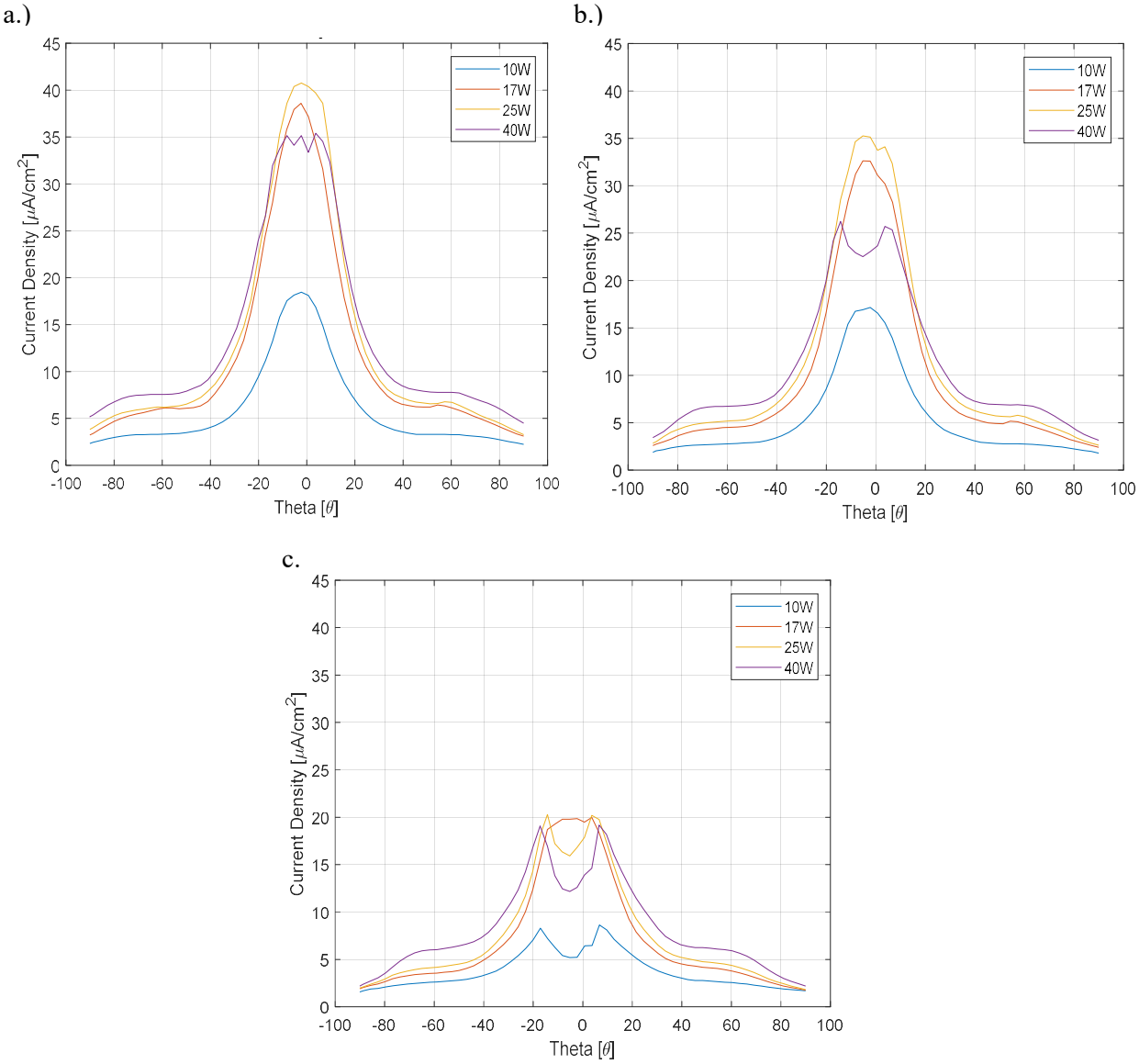

Figure 31: Angular current density profiles at a.) 1.5 SCCM, b.) 1.0 SCCM, and c.) 0.5 SCCM for respective absorbed power.

In the following some of the observed trends and features occurring in the above traces are discussed. An interesting result occurs at a 40 W of absorbed microwave power for all flow rates. More significantly Figure 31 (b) and (c) clearly shows a dip occurring at the central axis and slight bumps in the wings of each trace. The dip in the central axis of the thruster could be a result of the physical geometry of the inner conductor causing ions to diverge away from the central axis. At 1.5 SCCM the additional presence of greater ion current partially fills this dip resulting in the flatter peak seen in this trace. While in the 1.0 and 0.5 SCCM traces the lower ion current produced leads to the dip. Additionally, the divergence of ion current could be linked to the electric field pattern formed by the monopole antenna forcing the ions away from the central axis at higher powers. Interestingly the dip does not appear in the 17 W trace for all flow rates, and currently cannot be explained. The bump seen at the wings of the angular profile may arise from increased ionization occurring in the region near the radial walls, where neutral gas injection occurs in place of the central axis. Alternatively, this could result from charge exchange collisions resulting from higher energy particles at lower flow rates. This is supported by the RPA measurements in the following sections, but not the previous mean free path estimates.

The total ion current and mass utilization can be estimated through the integration of the current density profiles. These parameters are found for three xenon flow rates at four selected absorbed microwave powers. Figure 32 details these parameters for the monopole antenna. As expected, a steady increase in the amount of ionized propellant results from increasing microwave power with the greatest mass utilization occurring at the lowest flow rate. It is practical to assume a higher mass utilization would be achievable with a greater increase in microwave power. Total ion current rises as microwave power increases with the greatest increase occurring between 10 W and 17 W. A steady increase in total ion current is seen with microwave power starting at 17 W

for both mass utilization and ion current. This behavior is expected to continue as microwave power is further increased but may begin to saturate. Greater ion current is measured at higher flow rates due to the fact of more propellant being present with the potential to be ionized. The maximum ion current of approximately 50 mA is observed at 40 W of absorbed power and 1.5 SCCM. Comparing the traces from Figure 31 and Figure 32 for the respective flow rates, the highest mass utilization occurs at 40 W of absorbed power in the trace where the dip in the central axis is present. The high mass utilization measured in the 0.5 SCCM trace is indicative of the presence of doubly charged ions and is in the need of correction.

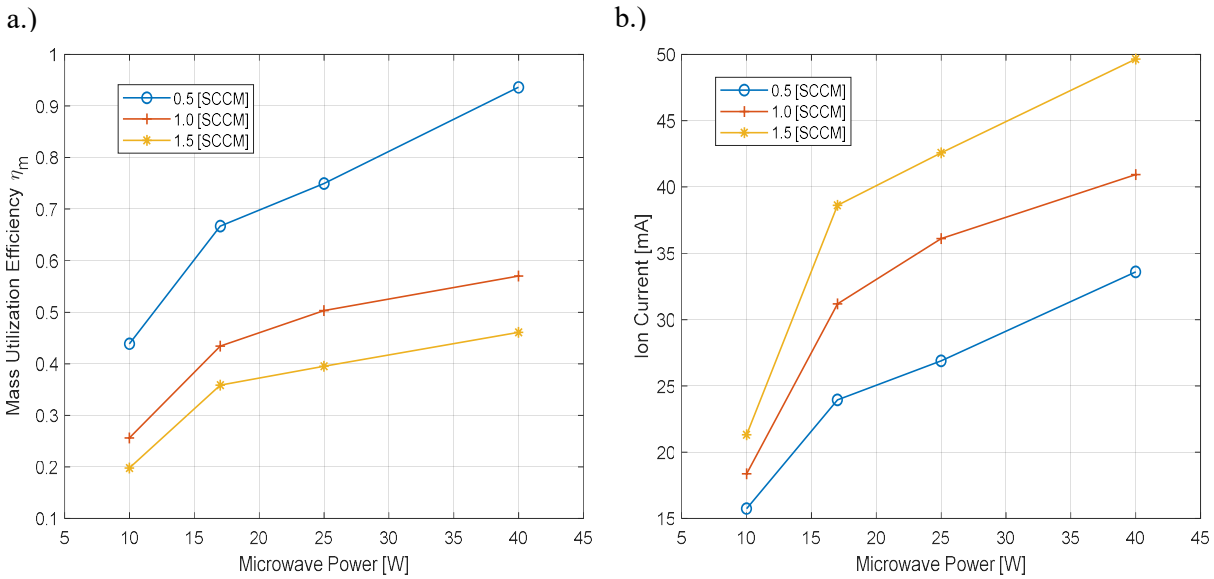

Figure 32: a.) Mass utilization and b.) total ion current monopole antenna.

As mentioned, issues occurred for operating the helical antenna above 30 W. Therefore, only three data points are provided for each flow rate. Without the additional data point, it is more difficult to comment on the behavior of the helical antenna traces. The angular current density traces for the helical antenna are displayed in Figure 33. Notably, the dip in the current density along the thruster centerline is not present in the figures. This possibly resulted from the open

physical geometry of the helical antenna as opposed to the straight rod of the monopole antenna. This allows ion current to be collected along the centerline removing the presence of the dip.

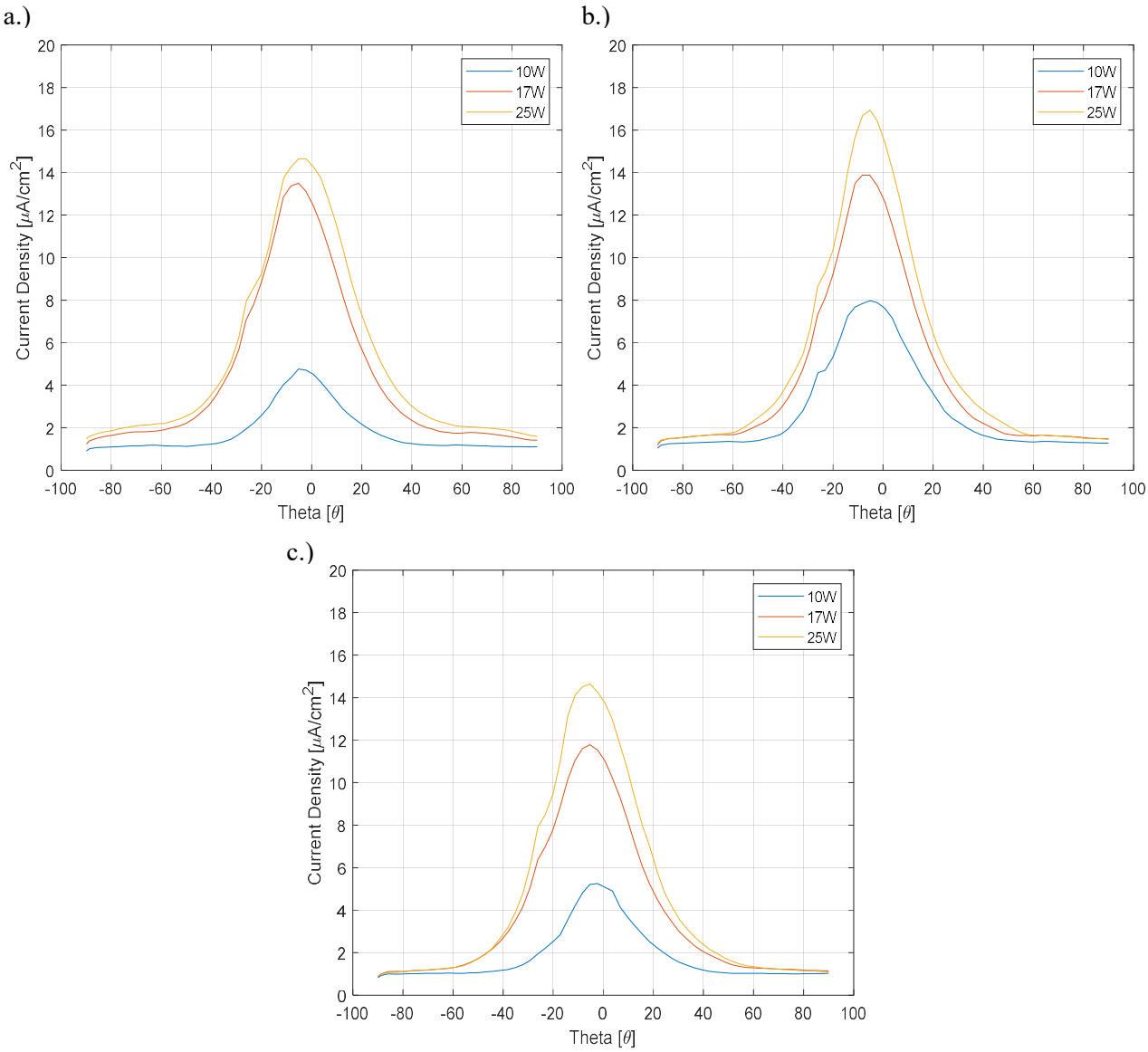

Figure 33: Helical antenna angular current density profiles a.) 1.5 SCCM, b.) 1.0 SCCM, and c.) 0.5 SCCM.

Figure 34 displays the total ion current and mass utilization for the helical antenna and shows poor performance when compared to the monopole antenna. The greatest increase in ion current and mass utilization still occurs when power is increased from 10 W to 17 W, and it is expected all traces will possess a linear behavior from 17 W and above. Figure 34 (b) at 10 W for 1.0 SCCM and 1.5 SCCM possess a notable result. A greater ion current is measured at 1.0 SCCM

than 1.5 SCCM. This unexpected result likely occurred due to possible wear on the helical antenna or fluctuations in absorbed power. When comparing the helical antenna to the monopole antenna, the helical performed substantially worse. The maximum estimated mass utilization at 0.5 SCCM and 25 W was above 75% for the monopole antenna while the helical antenna was just under half reaching only 36%. Additionally, the maximum ion current reached by the helical antenna was 17 mA, less than half of what was measured with the monopole antenna.

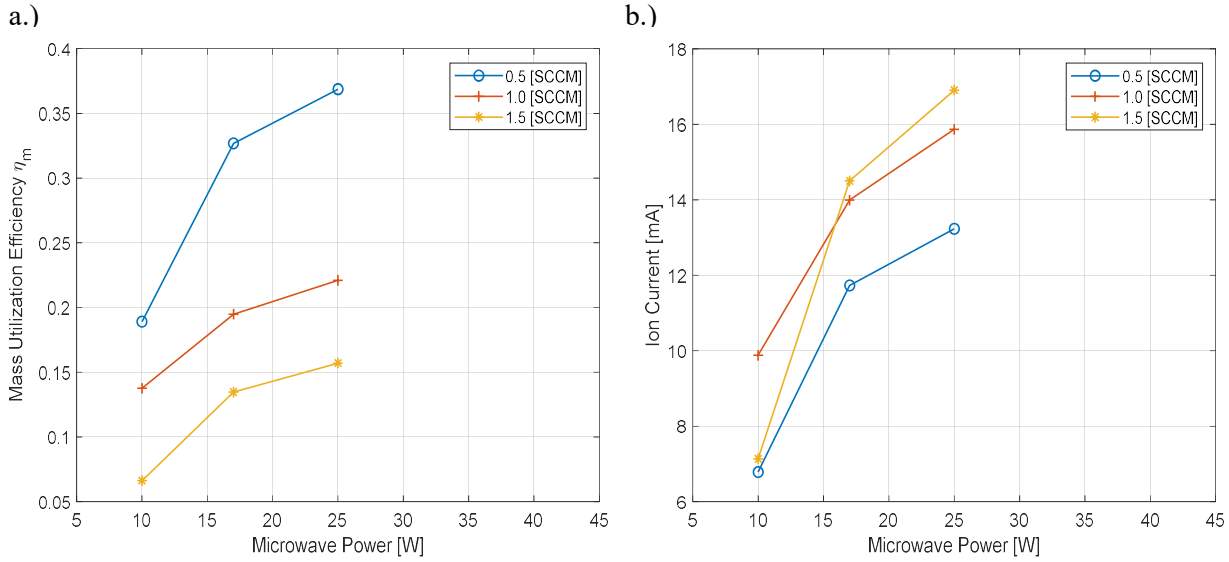

Figure 34: a.) Mass utilization and b.) total ion current of helical antenna.

The poor measurements obtained for total ion current and mass utilization for the helical antenna may be a result of several possibilities related to the antenna design and are discussed in section 5.2.3. Future work will look to improve upon these shortcomings.

5.2.3 Retarding Potential Analyzer

RPA measurements permit the mean ion energy to be calculated allowing the remaining thruster parameters to be estimated. As described in section 4.2.3 an RPA enables the IEDF to be determined from which the mean ion energy can be found. Figure 35 shows the normalized IEDF for the monopole antenna at the flow rates of 1.5 SCCM and 1.0 SCCM for various powers. To note, measurements at 0.5 SCCM are not included for large negative currents were recorded at all power levels, resulting in inaccurate data. The mean energy of each trace occurs near the peak of the IEDF. As seen between Figure 35 (a) and (b) decreasing flow rate results in an overall increase in ion energy, and as expected, ion energy also scales with microwave power. Greater ion energies occur at lower flow rates since there is lower pressure inside the source chamber. At higher flow rates more collisions occur resulting in ion energy lost to collisions. This is evident in the IEDF traces for each flow rate.

a.) b.)

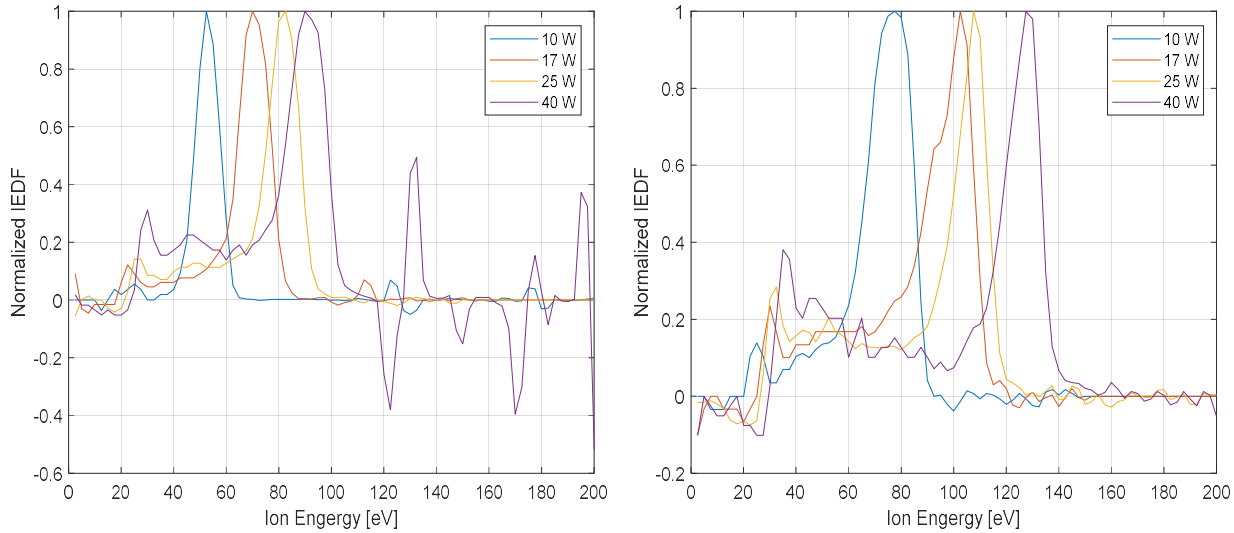

Figure 35: Ion energy distribution function for monopole antenna at (a) 1.5 SCCM and (b) 1.0 SCCM.

A jump in each IEDF resulting in a small peak is noticed at all power levels at lower ion energies between 20 – 40 eV. This is possibly the result of secondary electron emission from the background gas and RPA grids. The smaller peaks at high energies seen in the 1.5 SCCM 40W

trace likely results from power fluctuations from the microwave source. In comparison to work completed at ONERA [14,17] where ion energies reached ~250 – 300 eV at approximately 1 SCCM, the ion energies recorded here are considerably lower reaching a maximum of 127.5 eV at 1 SCCM. A possible reason for the lower energies observed in testing of the WECR thruster is the higher background pressure. Background pressure can have significant effects on magnetic nozzle performance [32, 33]. The experiments conducted in this thesis were performed at a background pressure approximately an order of magnitude greater than those in the aforementioned study at ONERA. The lower ion energy observed in Figure 35 can be attributed to the higher background pressure leading to a greater collision rate and lower ion energy.

The IEDFs obtained for the helical antenna are displayed in Figure 36. Compared to the IEDFs from the monopole antenna, the helical antenna mean ion energies are typically ~ 10 – 20 eV lower. Similar trends with flow rate and microwave power are observed in the helical antenna IEDF as with the monopole antenna. At lower ion energies before the maximum peak of the IEDF, a bump appears in the traces which does not appear in the monopole IEDF. This bump shows a larger lower energy ion population in comparison to the monopole antenna. Currently this bump cannot be explained but it is thought to be caused by elastic collisions, charge exchange collisions, and low energy ions created downstream [33-35].

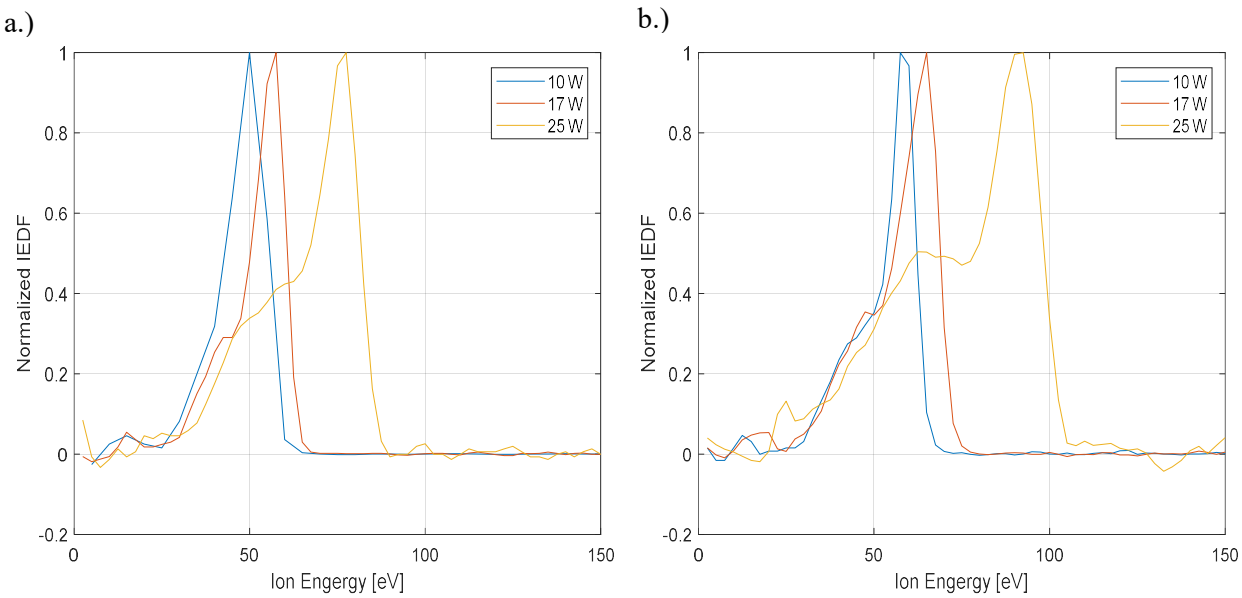

Figure 36: IEDF for helical antenna (a) 1.5 SCCM and (b) 1.0 SCCM.

As stated, to estimate thrust, the mean ion velocity is required and with the ion energies obtained from the IEDF the velocities can be found. The ion velocity is proportional to ion energy and exhibits the same trends with flow rate and power as seen in the IEDF's. The calculated ion velocities of the monopole and helical antenna are shown in Figure 37. Observing Figure 37 a.), it appears the ion velocity begins to level off the further microwave power is increased. The helical antenna however shows a significant increase from 17W to 25W and may not approach a limit early as the monopole antenna.

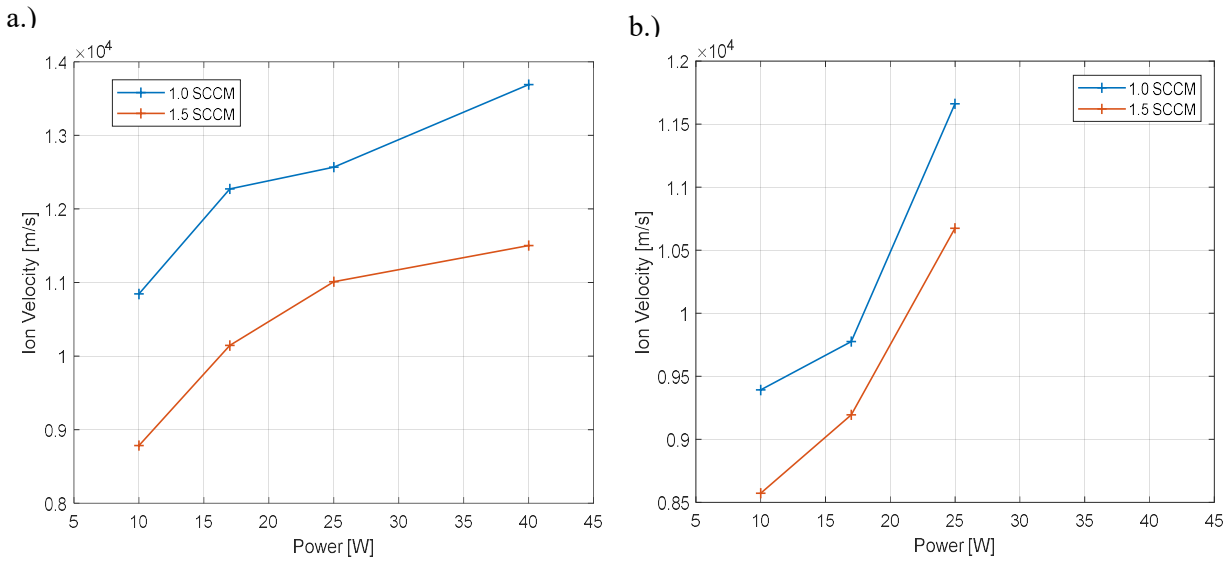

Figure 37: Ion velocity measurements for 1.0 and 1.5 SCCM at various absorbed microwave powers for (a) monopole antenna and (b) helical antenna.

The greatest ion energy and therefore ion velocity is obtained with the monopole antenna at 1.0 SCCM. It was previously thought the helical antenna would outperform the monopole antenna leading to greater ion energies. This initial reasoning was based on the helical antenna's capability to produce RHCP waves. The fabrication method of the antenna may have caused poor performance of the helical antenna. A new fabrication method is needed along with a more detailed design process. It is possible the antenna did not produce RHCP waves, or the waves did not propagate through ECR region, leading to an ineffective design. To test if RHCP waves were produced it is possible to a secondary linearly polarized antenna acting as a receiver. The receiving antenna is rotated and records power measurements from the antenna under test [36]. From these measurements the polarity of the antenna under test can be determined. The antennas were originally fabricated by hand to obtain the desired design parameters. Future testing could include an antenna whose fabrication is outsourced to achieve a more accurate performance. A summary of the mean ion energies obtained from RPA testing is displayed in the table below.

Table 2: Ion energies at various microwave powers for the monopole and helical antennas.

Flow Rate	Power	Monopole	Helical
1.0 SCCM	10 W	80 eV	60 eV
1.0 SCCM	17 W	102.5 eV	65 eV
1.0 SCCM	25W	107.5 eV	92.5 eV
1.0 SCCM	40 W	127.5 eV	NA
1.5 SCCM	10 W	52.5 eV	50
1.5 SCCM	17 W	70 eV	57.5
1.5 SCCM	25W	82.5 eV	77.5
1.5 SCCM	40 W	90 eV	NA

5.3 Thruster Performance

In the following sections the full characterization of the WECR thruster is discussed. The thrust, $I_{sp,}$ and efficiency parameters are given for both antenna configurations. Additionally, a brief discussion on the effects of background pressure on thruster performance is provided along with a section on how transmitted and reflected microwave power varied throughout experimentation.

5.3.1 Performance Evaluation

Presented in this section is the accumulation of data obtained from the testing discussed previously, allowing the thruster performance to be characterized. Data measured with the FC and RPA allow for the estimation of thrust, I_{sp}, and all thruster efficiency parameters. These estimations are only made for 1.0 and 1.5 SCCM for RPA measurements were not made at 0.5 SCCM. First, the thrust and I_{sp} are given by equations 4.7 and 4.12. These estimations are displayed in Figure

38 for the monopole antenna and Figure 39 for the helical antenna. There is negligible difference in the amount of thrust measured at 1.0 and 1.5 SCCM with the monopole antenna. This may be due to the inverse relationship between ion energy and total ion current due to flow rate. While the ion energy produced at lower flow rates is greater due to a lower pressure inside the source chamber, the amount of total ion current produced is lower as well due to less neutral gas to be ionized. A greater difference is present for I_{sp}, as the decrease in flow rate permits a higher I_{sp}. The optimum operating condition appears to be at an intermediate flow rate to balance both total ion current and ion energy.

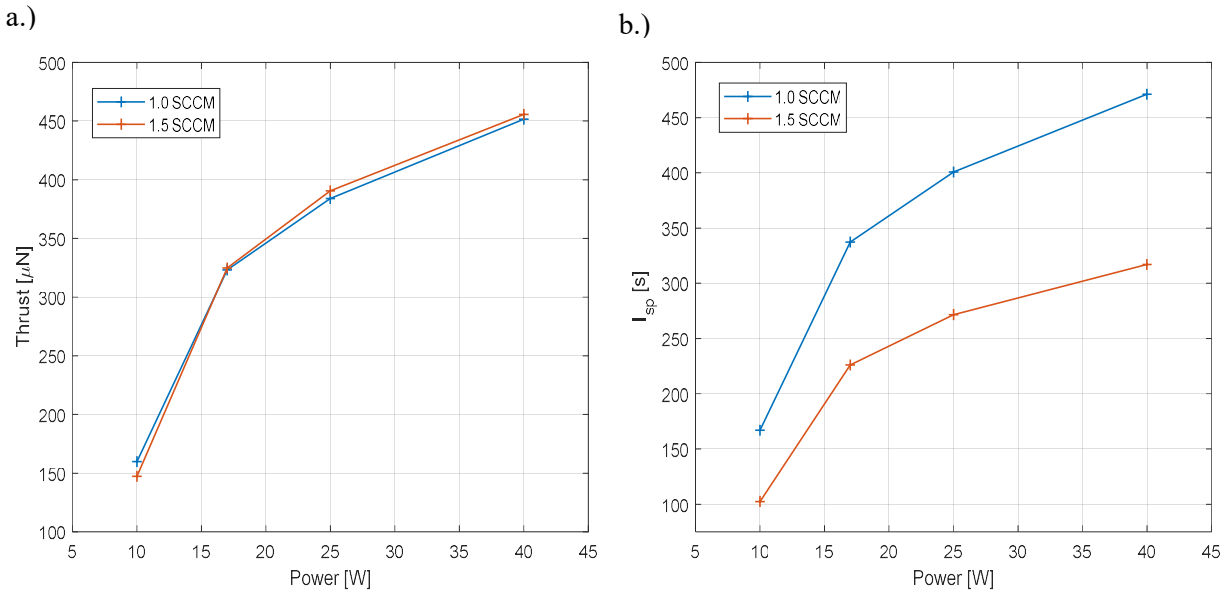

Figure 38: (a) Thrust and (b) specific impulse measurements of monopole antenna at 1.0 and 1.5 SCCM for varying absorbed microwave power.

The thrust and I_{sp} for the helical antenna show a severe decrease in both record values compared to the monopole antenna. The low thrust and I_{sp} is most likely the result of poor microwave plasma coupling from the antenna design. Both thrust and I_{sp} increase with microwave power and do not begin to saturate under 25 W. It is possible better performance could be achieved at higher microwave powers. COMSOL simulations discussed in section 3.5 showed the helical antenna would result in poor performance due to an insufficient electric field pattern creating numerous $E \times B$ points. The antenna design method proved to be an effective technique to estimate

the performance of an antenna. However, it is still believed a RHCP wave antenna would lead to improved performance. A new RHCP wave antenna configuration could possibly correct the faults in this design.

a.)

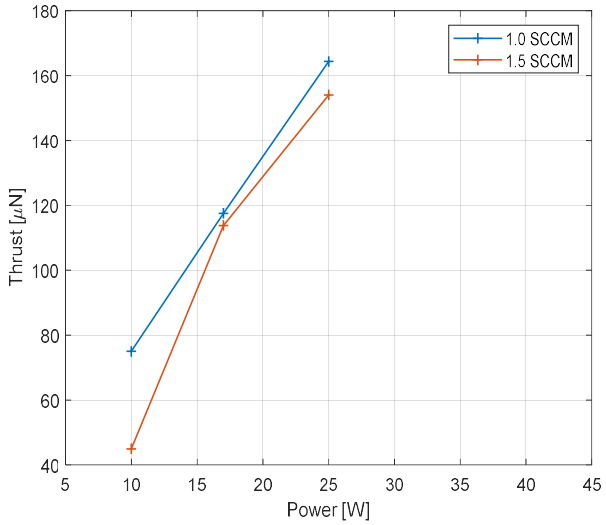

b.)

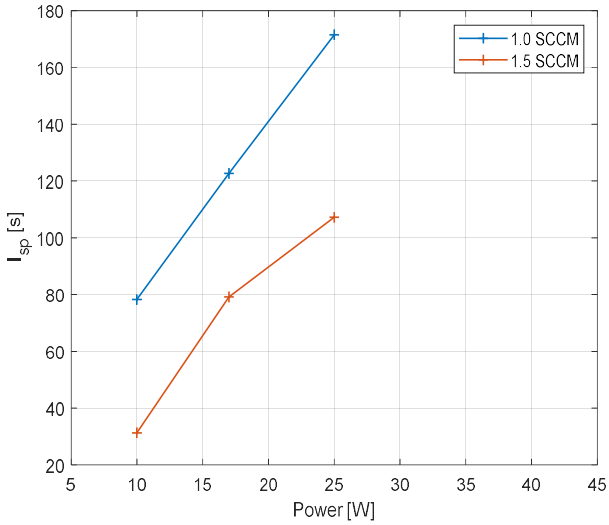

Figure 39: (a) Thrust and (b) specific impulse measurements of helical antenna at 1.0 and 1.5 SCCM for varying absorbed microwave power.

Figure 40 displays the calculated efficiency parameters for both the monopole and helical antennas at 1 SCCM. This is considered the most optimal operating condition for there is a balance between total ion current and ion energy. At this condition the monopole antenna achieved a maximum total efficiency of $\eta_T = \sim 3.2\%$ at 17 W, while the helical antenna achieved a mere $\eta_T = \sim 0.5\%$ at 25 W. From these figures it is observed that all efficiency parameters appear to saturate with increasing microwave power. It is evident that increasing microwave power does not necessarily result in increasing the efficiency of the thruster; rather there is some mechanism. From references [6, 19, 20, 21] losses to the radial walls have been known to be a significant problem and is a limiting factor in the efficiency of the thruster. The magnetic field configuration chosen for the WECR thruster may not have resulted in the effective confinement of the plasma as previously

thought. A method not implemented in the WECR thruster but was shown to have great performance benefits is insulating walls. This is considered in a future design [37].

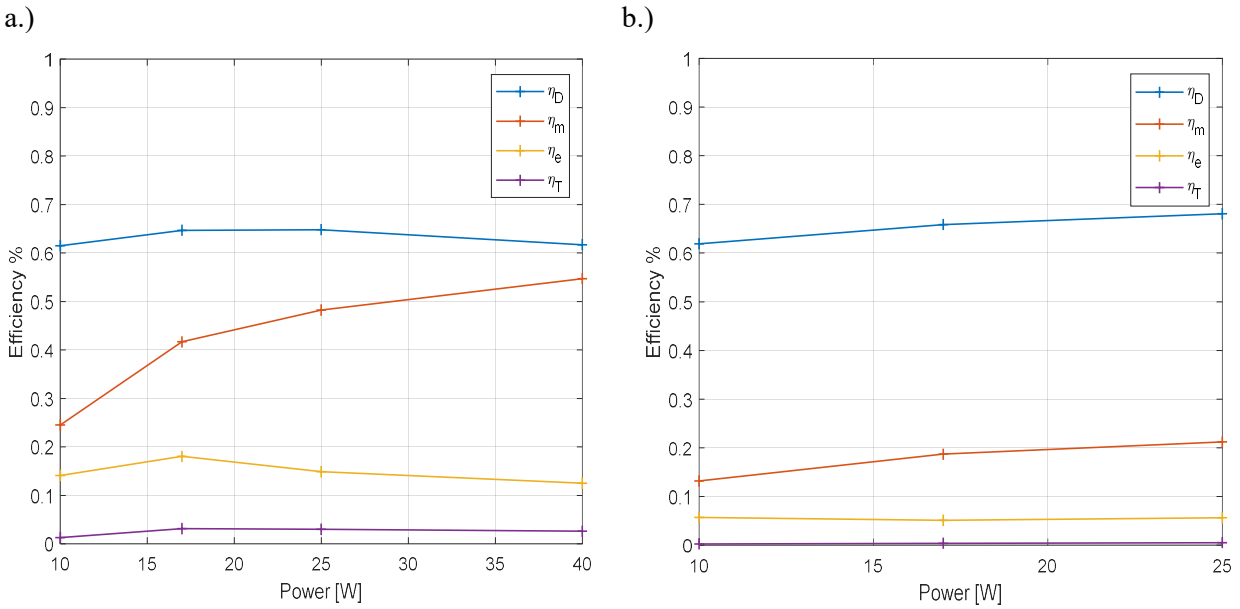

Figure 40: Efficiencies at 1 SCCM for the (a) monopole antenna and (b) helical antenna.

Equations 4.8, 4.9, and 4.10 detail a few select ways to improve upon the efficiency of the thruster without introducing additional gas flow or microwave power. Mass utilization, divergence factor, and energy efficiency can all be improved with an increase in total ion current. In addition to increasing total ion current, the divergence factor and energy efficiency can also be improved with greater ion energies. Alterations in the magnetic field could potentially lead to increased ion energy and total ion current without having to alter the flow rate or microwave power to the thruster. The ion energy is linked to electron temperature, and it has been shown that different magnetic field configurations can increase the measured electron temperature, ion energy, and current density [18,29]. Improvements to these metrics could have significant performance benefits. Overall, several design improvements could be made along with more ideal operating conditions allowing the WECR thruster to achieve improved efficiencies.

5.3.2 Background Pressure Effects

Past studies on ECR thrusters and magnetic nozzle-based thrusters have shown that these devices are significantly affected by background pressure [15,32,33]. Although, no direct study on background pressure effects was carried out in this work, pressure measurements were recorded throughout testing of the WECR thruster. These measurements manifested notable effects RPA measurements. RPA data was collected with the WECR thruster at operating pressures around an order of magnitude greater than in previous studies [17], leading to a significant decrease in ion energy measurement. All FC and RPA measurements were made with background pressure on the order of 1e-5 Torr. For comparison in previous studies, at approximately 5e-5 Torr a total efficiency of $\eta_T = \sim 10\%$ is achievable while around 1e-4 Torr $\eta_T = \sim 2\%$ [15]. It is believed if lower pressures were attainable, measured ion energies would range from 200-300 eV. Overall, background pressure can have a significant effect on the performance of magnetic nozzle thrusters such as ECR thrusters. Facilities capable of obtaining operating pressures below 1e-5 Torr are preferred.

5.3.3 Transmitted and Reflected Power

Throughout testing of the WECR thruster both transmitted and reflected power were monitored and recorded at various powers and flowrates to observe behavior. Transmitted and reflected power varied for both antenna configurations. The antenna configuration and operating pressure had the most significant effect on microwave plasma coupling. Testing of the monopole antenna led to relatively constant reflected power levels with very little variation at all operating conditions. When testing the helical antenna, reflected power levels fluctuated quite substantially leading to erroneous data and energy spikes as seen in the RPA measurements. Although the reflected power remained low at the beginning of an experiment, over time, it would begin to rise

and fluctuate, causing power spikes. This occurred in the monopole antenna but was not as profound as for the helical antenna. The rise in reflected power and fluctuations is most likely a result of poor impedance matching to the plasma and heating of the microwave cables over time.

As discussed in section 4.1.3 a double stub tuner was utilized for impedance matching. This tool allowed the impedance of the microwave circuit to match that of the plasma by adjusting two stubs. The tuner was adjusted before each plasma diagnostic experiment to best match the impedance of the plasma with the microwave circuit. While this double stub tuner was adjusted manually, an automatically adjusted system, similar to those in impedance matching circuits for waveguides, which could match the circuit impedance to the plasma as it operates would be most beneficial. This would allow for the most optimized method for ensuring maximum absorbed and minimum reflected power.

An important result noticed after the testing of each antenna configuration is small amounts of erosion caused by sputtering. An advantage of ECR thrusters previously discussed was increased lifetimes [5]. However, an exposed antenna to the plasma as used in ECR thrusters, can slowly deteriorate due to sputtering becoming a life limiting factor. The erosion of the antenna could also lead to negative effects on transmitted and reflected power due to the deterioration of the antennas physical geometry changing its impedance. The antenna used in this work consisted of copper which possess a sputtering yield that is typically greater than other metals for noble gas ions [38, 39]. Small amounts of material could be observed to be absent along with surface imperfections after experimental testing periods. The sheath potential can be an indicator for determining the scale of erosion. However, potentials in the region near the antenna could not be estimated for no electron temperature measurements were conducted near this location. While no lifetime estimations were completed, and no relevant data could be sourced at the desired ion

energies to estimate the lifetime of the antenna, this is an issue needing investigation. To decrease the amount of erosion an antenna material with a lower sputtering yield such as refractory metals can be chosen [40] Alternatively, the antenna could be coated with a low sputtering yield dielectric as used in a water based ECR thruster [41]. This would aid in the transfer of microwave power throughout the testing of the thruster and increase the overall lifetime of the thruster.

5.4 WECR-2 Thruster Design

As previously iterated, the efficiency of small scale ECR thrusters have been relatively poor with a maximum total efficiency of ~16% [5]. Comparing this value to the total efficiency obtained with the WECR thruster $\eta_T = 3.2\%$, room for improvement is undoubtedly present in the first design iteration of the thruster. The results obtained from the aforementioned plasma diagnostic tests have informed on design flaws in the WECR thruster, revealing potential improvements. Discussed here are the design changes used in the second iteration of the WECR thruster. To distinguish the designs from each other, the first thruster design is WECR-1 and the second is WECR-2. The second design iteration of the thruster is displayed in Figure 41 with each component called out in the CAD model.

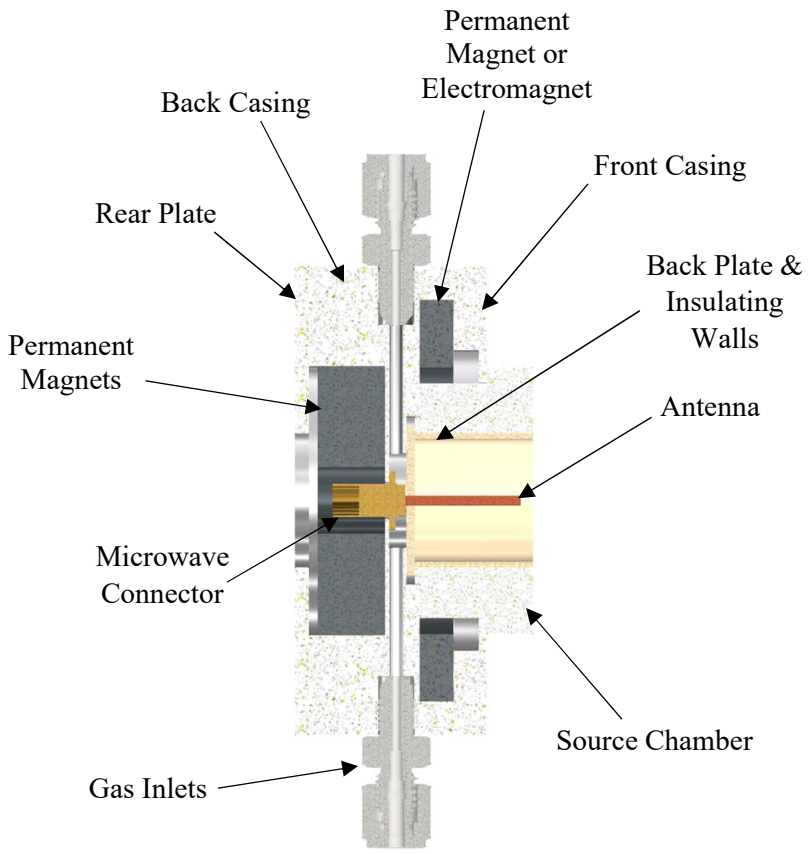

Figure 41: WECR-2 thruster optimized design CAD model.

As stated, the WECR-1 thruster utilized radial gas injection with two permeant magnets. The WECR-2 thruster will employ axial gas injection and has the capacity to utilize either three permanent magnets or replace the third with a solenoid. A benefit of utilizing axial injection over radial, is that it enables the backplate to be used as a mechanism to distribute gas into the source chamber and can provide a more uniform distribution. A uniform distribution can be accomplished through the design of the backplate as various patterns can be cut into the ceramic plate altering distribution of the neutral gas.

Below in Figure 42 the simulated magnetic field pattern of the WECR-2 thruster, with the addition of a third permanent magnet located outside of the source chamber, is displayed. Comparing the field patterns, the addition of the third magnet forms a more axial pattern causing

the field lines to diverge away from the source chamber walls. The third permanent magnet improves field line termination at the radial walls but creates an overall weaker magnetic field. The effect of the addition of the third magnet could possibly be negative in terms of wall losses but beneficial for plasma detachment. If in place of the third permanent magnetic a solenoid was used, there would be greater adaptability to influence the magnetic field gradient. This would enable a larger ECR region where electrons would possess a greater residence time within the region gaining more energy. A similar investigation was conducted where the magnetic field configuration was set up using a solenoid and one permanent magnet showing an improved mass utilization and divergence factor could be achieved while operating at lower flow rates [18]. The WECR-1 thruster was designed without a solenoid so that it would only require a single power source. In this configuration the simulated ECR region would be located exactly at the backplate. Taking into account the same differnce as measured with the gauss meter in the WECR-1 thruster this places the ECR region 2-3 mm from the backplate.

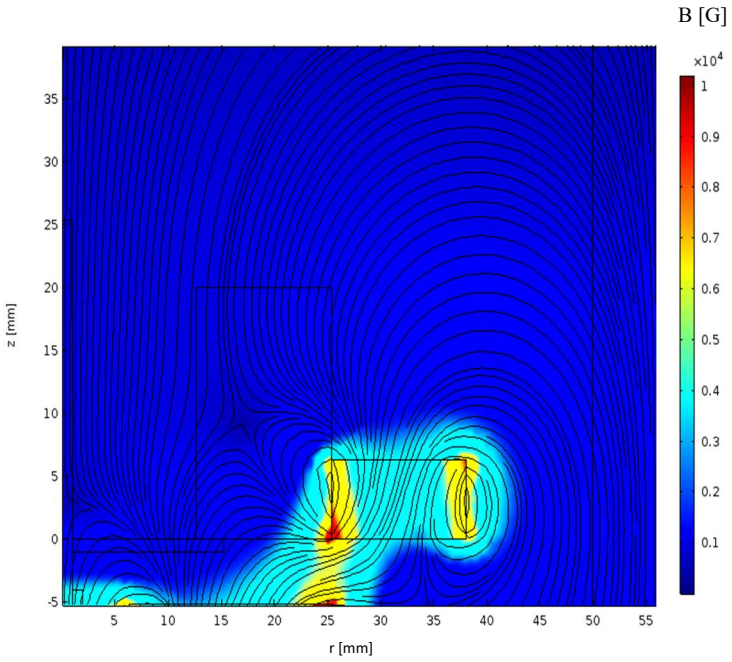

Figure 42: WECR-2 magnetic field pattern with additional permanent magnet.

The internal geometry of the source chamber of both designs remains constant. Although alterations in the diameter and length of the source chamber would likely show improvements as a result of the decrease in chamber pressure, keeping the geometry constant in each design allows for direct comparison to the other design changes mentioned. To hold the additional permanent magnet or solenoid, an external casing is incorporated into the WECR-2 thruster. The new and old casings containing the magnets were increased to 3.5” in diameter. As stated, the source chamber dimensions will remain constant with a 1” inner diameter and a length of 0.9”. These dimensions directly impact the overall performance of the thruster as discussed above and in section 3.2. Lastly, insulating the source chamber walls could significantly reduce wall losses and improve overall efficiency [37]. Insulation of the walls can be accomplished through a protective layer of dielectric material similar to the backplate material. Improvement in total efficiency as a result of wall insulation is thought to be a consequence of two possible mechanisms. First, the insulated walls alter the secondary electron emission, changing the electron balance within the source chamber plasma. Secondly, conducting source chamber walls can affect diffusion to the walls, by insulating the walls better confinement is achieved [3]. The combination of these two possible effects could lead to a substantial improvement in the efficiency of the thruster.

The plasma diagnostic tests performed on the WECR-1 thruster informed on where potential improvements could be incorporated. From the experiments, conducted the most significant methods to potentially improve upon the WECR-1 thruster’s performance are alterations to the magnetic field and operating conditions such as background pressure. First, Langmuir probe testing provided insight into the importance of initial conditions in particular flow rate and how the plasma properties are related to the performance of the thruster when examined with collected data from the remaining tests. For example, in a previous study it was shown that

the shape of the ambipolar electric field is affected by the initial conditions present in the thruster [31]. Here it appears that the flow rate and base pressure throughout experimentation have a particular effect on the plasma potential and electron temperature. Both electron temperature and plasma potential profile are key to the performance of the thruster. In conjunction with the Langmuir probe measurements, the RPA tests showed a relationship between flow rate, maximum ion energy, and electron temperature. This relationship was verified by both RPA and Langmuir probe tests show that at lower flow rates greater electron temperature and ion energies were measured. Both ion energy and electron temperature increase with decreasing flow rate for the reasons discussed in section 5.2.3. A higher electron temperature will lead to greater ion energy and therefore more thrust, but at lower flow rates, less thrust is produced due to the lack of potential propellant to be ionized. Both electron temperature and ion energy can be enhanced through magnetic field manipulations as shown by Lafleur et al [29]. In addition to the magnetic field alterations, the backplate could be re-designed to lead to more effective gas distribution. This could also improve upon electron temperature and ion energy resulting in improvements with the WECR-2 thruster.

Additional changes that should be implemented into the WECR-2 thruster include a new antenna fabrication method to improve upon antenna durability and repeatability, helical antenna redesign to increase/improve microwave plasma coupling, and insulated walls. It is believed the changes mentioned in this section will improve upon the performance of the WECR-1 thruster, creating a design on par with current ECR thruster designs [17,18,37].

CHAPTER 6

SUMMARY AND FUTURE WORK

6.1 Summary

The goal of this work was to design and optimize an ECR thruster while also providing additional experimental data on ECR thrusters. This work began with the design of an ECR thruster in ALPE at Western Michigan University. This design was based on the coaxial ECR thruster developed at ONERA labs [5]. The dimensions of the WECR-1 thruster were informed by previous experimental work with ECR thrusters and were chosen to produce an effective thruster [14,15]. In creating an effective design, this work utilized a method for the optimization of microwave antenna designs in ECR ion thrusters [16]. Three antenna configurations were initially simulated and tested including a monopole, ring, and helical antenna. Only two of the three antenna designs were experimentally characterized, the monopole antenna as used in previous ECR thrusters and the helical antenna, which was expected to produce RHCP waves to heat the electrons more efficiently. One of the most important features of the ECR thruster is the magnetic nozzle. The magnetic nozzle aids in the creation, confinement, and acceleration of the plasma. To create an optimum field for both plasma confinement and detachment, magnetic field simulations were conducted showing the magnetic vector field and field strength. Magnetic field probe measurements were completed to verify the simulations showing relatively good agreement. The last design feature investigated was possible improvements to the ECR region by reducing the magnetic field gradient or by improving microwave plasma coupling.

The WECR-1 thruster was characterized through the use of a series of plasma diagnostic experiments including Langmuir probe tests for plasma potential, electron density, and electron temperature measurements, FC tests for the total ion current produced by the thruster, and RPA

measurements for ion energy. With the data from these diagnostics thruster efficiency parameters could be calculated along with thrust and I_{sp} produced by the thruster. Langmuir probe testing resulted in both antennas possessing similar values in plasma potential and electron temperature; however, the monopole antenna possessed a significantly greater rate of increase in electron density with changing flow rate when compared to the helical antenna. FC tests showed the monopole antenna was much more capable of ionizing the gas compared to the helical antenna with the monopole producing a maximum total current of 50 mA while the helical antenna only produced a maximum current of 17 mA. Lastly, RPA measurements showed the monopole antenna was more efficient at creating high energy ions then the helical antenna. Compared to previous studies conducted with ECR thrusters achieving ion energies of ~250-300 eV these values were significantly lower achieving a maximum of 127.5 eV [14,17]. The lower ion energies are partly attributed to a higher operating pressure throughout testing. The thrust and I_{sp} calculated for the monopole antenna were respectively 0.41 mN and 471 s at 40W and 1 SCCM. While the maximum I_{sp} was achieved at these conditions the maximum thrust was measured at 40 W and 1.5 SCCM. The maximum thrust and I_{sp} for the helical antenna came in at poor values of 0.16 mN and 171 s operating at 25 W and 1 SCCM. The maximum total efficiencies obtained for each antenna configuration at 1 SCCM were $\eta_T = 3.2$ % at 17 W for the monopole and the helical antenna $\eta_T = 0.5$ % at 25 W. While these values are low, the WECR-1 thruster operating with the monopole antenna is similar to the first design iteration of previous ECR thrusters [17,18,37]. From these experimental results, a second design was developed to improve on the WECR-1 thruster. The second design, simply deemed WECR-2 thruster, consisted of the same source chamber geometry. Maintaining geometric parameters allows for a more direct comparison.

Three major changes were made to the WECR-1 thruster. First, the gas injection scheme was changed from radial to axial. Second, an additional section was added to the thruster external geometry to allow for a third permanent magnet or solenoid to be incorporated. This will aid in increasing the total ion current, electron temperature, and therefore ion energy, increasing thruster efficiency. Finally, a dielectric material will be used to insulate the thruster walls, to increase performance. It is believed with the combination of the above changes to the WECR-1 thruster, the WECR-2 thruster will show improved performance with total efficiency closer to ~10%.

6.2 Future Work

A more complete understanding of the physics behind ECR thrusters, specifically magnetic nozzles and microwave plasma coupling, is required for ECR thrusters to be considered as a viable alternative to existing electric propulsion technologies. This work has provided experimental data with the hope of aiding in the advancement of ECR thrusters. The same series of experiments should be conducted with the WECR-2 thruster with the goal of greatly improving upon the efficiency of its predecessor. When testing is completed with WECR-2 thruster experimental investigation into the effect of neutral gas distribution and different magnetic field configurations could be carried out. Additional experimental research can be conducted into pressure effects, microwave plasma coupling, and plasma detachment in ECR magnetic nozzle thrusters with the WECR-2. While this work was primarily an experimental investigation with select multiphysics simulations, theoretical and numerical work is needed to better understand the physics of ECR thrusters. The miniaturization of EP thrusters will play a vital role in the future of the space industry, specifically CubeSat constellations requiring a propulsion system. ECR thrusters possess the potential to compete with the performance and capabilities of HETs and GITs. Electric

propulsion is an ever-growing field with great potential, and with a growing space industry, ECR thrusters could play a significant role.

REFERENCES

[1] Webb-Mack, Z. (2018). *A Brief History of Ion Propulsion*. Retrieved from NASA Science Solar System Exploration: https://solarsystem.nasa.gov/news/723/a-brief-history-of-ion-propulsion/

[2] Goebel, D. and Katz, I. (2008). *Fundamentals of Electric Propulsion: Ion and Hall Thrusters*. Hoboken, NJ: John Wiley & Sons, Inc.

[3] Levchenko, I., Xu, S., Mazouffre, S., Lev, D., Pedrini, D., Goebel, D., Garrigues, L., Taccogna, F., & Bazaka, K. (2020). Perspectives, frontiers, and new horizons for plasma-based space electric propulsion. *Physics of Plasmas*, *27*(2), 20601. https://doi.org/10.1063/1.5109141

[4] Jahn, R. (2006). *Physics of electric propulsion / Robert G. Ja illustrations by Woldemar von Jaskowsky.* Dover Publications, Inc.

[5] Packan, D., Elias, P.-Q., Jarrige, J., Correyrto, S., Peterschmitt, S., Porto-Hernandez, J.-C., Merino, M., Sánchez-Villar, A., Ahedo, E., Peyresoubes, G., Thorinius, A., Denis, S., Holste, K., Klar, P., Scharmann, S., Zorn, J., Bekemans, M., Scalais, T., Bourguignon, E., Zurbach, S., Azais, P., Habbassi, I., Mares, M., and Hoque, A. (2019). H2020 MINOTOR: Magnetic Nozzle Electron Cyclotron Resonance Thruster. Presented at the 36th International Electric Propulsion Conference, University of Vienna, Vienna, Austria.

[6] Popov, O. A. (1995). *High density plasma sources design, physics, and performance / edited by Oleg A. Popov.* Noyes Publications.

[7] Little, J. M., & Choueiri, E. Y. (2013). Thrust and efficiency model for electron-driven magnetic nozzles. *Physics of Plasmas*, *20*(10), 103501. https://doi.org/10.1063/1.4824613

[8] Merino, M., & Ahedo, E. (2017). Space plasma thrusters: Magnetic nozzles for. *Encyclopedia of Plasma Technology*, *2*, 1329-1351.

[9] Martinez, M. (2013). Analysis of Magnetic Nozzle For Space Plasma Thrusters. [Doctoral dissertation, Polytechnic University of Madrid]

[10] F. Ebersohn, S. Girimaji, D. Staack, J. Shebalin, B. Longmier, & C. Olsen. (2012). Magnetic Nozzle Plasma Plume: Review of Crucial Physical Phenomena. In *48th AIAA/ASME/SAE/ASEE Joint Propulsion Conference & Exhibit*. https://doi.org/10.2514/6.2012-4274

[11] Navarro-Cavall´e, J., Correyer S., & Ahedo, E. (2015). Collisionless electron cooling on magnetized plasma expansions: advances on modelling. *Presented at Joint Conference of 30th International Symposium on Space Technology and Science, 34th International Electric Propulsion Conference and 6th Nano-satellite Symposium. Hyogo-Kobe, Japan.*

[12] Ahedo, E., & Merino, M. (2011). On plasma detachment in propulsive magnetic nozzles. *Physics of Plasmas*, *18*(5), 053504–053504–8. https://doi.org/10.1063/1.3589268

[13] Deline, Bengtson, R. D., Breizman, B. N., Tushentsov, M. R., Jones, J. E., Chavers, D. G., Dobson, C. C., & Schuettpelz, B. M. (2009). Plume detachment from a magnetic nozzle. *Physics of Plasmas*, *16*(3), 033502–033502–9. https://doi.org/10.1063/1.3080206

[14] Cannat, F., Lafleur, T., Jarrige, J., Chabert, P., Elias, P.-Q., & Packan, D. (2015). Optimization of a coaxial electron cyclotron resonance plasma thruster with an analytical model. *Physics of Plasmas*, *22*(5), 53503. https://doi.org/10.1063/1.4920966

[15] Vialis, T., Jarrige, J., & Packan, D. (2017). Geometry optimization and effect of gas propellant in an electron cyclotron resonance plasma thruster". *Presented at the 35th International Electric Propulsion Conference Georgia Institute of Technology, Atlanta, Georgia*

[16] Koizumi, H., & Kuninaka, H. (2009). Antenna Design Method and Performance Improvement of a Micro ion Engine Using Microwave Discharge. TRANSACTIONS OF THE JAPAN SOCIETY FOR AERONAUTICAL AND SPACE SCIENCES, SPACE TECHNOLOGY JAPAN https://doi.org/10.2322/tstj.7.Pb_89

[17] Jarrige, J., Elias, P., Packan, D., & Cannat, F. (2013). Characterization of a coaxial ECR plasma thruster. In *44th AIAA Plasmadynamics and Lasers Conference*. https://doi.org/10.2514/6.2013-2628

[18] Cannat, F., Jarrige, J., Elias, P., Packan, D. (2014). Experimental investigation of magnetic gradient influence in a coaxial ECR plasma thruster. Presented at the Space Propulsion 2014 Maritim Hotel, Cologne, Germany.

[19] Lafleur. (2014). Helicon plasma thruster discharge model. *Physics of Plasmas*, *21*(4), 43507. https://doi.org/10.1063/1.4871727

[20] Takahashi, Sugawara, T., & Ando, A. (2020). Spatial measurement of axial and radial momentum fluxes of a plasma expanding in a magnetic nozzle. *New Journal of Physics*, *22*(7), 73034. https://doi.org/10.1088/1367-2630/ab98d5

[21] Takahashi, Sugawara, T., & Ando, A. (2020). Spatially- and vector-resolved momentum flux lost to a wall in a magnetic nozzle rf plasma thruster. *Scientific Reports*, *10*(1), 1061–1061. https://doi.org/10.1038/s41598-020-58022-6

[22] Kawai, & Ueda, Y. (2000). Electromagnetic wave propagation in an ECR plasma. *Surface & Coatings Technology*, *131*(1), 12–19. https://doi.org/10.1016/S0257-8972(00)00771-4

[23] Lobbia, & Beal, B. E. (2017). Recommended Practice for Use of Langmuir Probes in Electric Propulsion Testing. *Journal of Propulsion and Power*, *33*(3), 566–581. https://doi.org/10.2514/1.B35531

[24] Valentin, & Stéphane, M. (2021). Optimization of a Faraday Cup Collimator for Electric Propulsion Device Beam Study: Case of a Hall Thruster. *Applied Sciences*, *11*(5), 2419. https://doi.org/10.3390/app11052419

[25] Brown, Walker, M. L. R., Szabo, J., Huang, W., & Foster, J. E. (2017). Recommended Practice for Use of Faraday Probes in Electric Propulsion Testing. *Journal of Propulsion and Power*, *33*(3), 582–613. https://doi.org/10.2514/1.B35696

[26] Hugonnaud, Mazouffre, S., & Krejci, D. (2021). Faraday cup sizing for electric propulsion ion beam study: Case of a field-emission-electric propulsion thruster. *Review of Scientific Instruments*, *92*(8), 84502–084502. https://doi.org/10.1063/5.0060931

[27] Ferda, B. (2015). Retarding Potential Analyzer Theory and Design. Princeton University.

[28] Baird, M., Kerber, T., Lemmer, K., & Huang, W. (2019). "Hall thruster plume measurements of time resolved ion energy," in 36th International Electric Propulsion Conference, Vienna, Austria.

[29] Lafleur, Cannat, F., Jarrige, J., Elias, P. Q., & Packan, D. (2015). Electron dynamics and ion acceleration in expanding-plasma thrusters. *Plasma Sources Science & Technology*, *24*(6), 65013. https://doi.org/10.1088/0963-0252/24/6/065013

[30] Correyero, Jarrige, J., Packan, D., & Ahedo, E. (2019). Plasma beam characterization along the magnetic nozzle of an ECR thruster. *Plasma Sources Science & Technology*, *28*(9), 95004. https://doi.org/10.1088/1361-6595/ab38e1

[31] Jarrige, J., Correyero, S., Elias, P., & Packan, D. (2017). Investigation on the ion velocity distribution in the magnetic nozzle of an ECR plasma thruster using LIF measurements. Presented at the 35th International Electric Propulsion Conference Georgia Institute of Technology, Atlanta, Georgia.

[32] Wachs, & Jorns, B. (2020). Background pressure effects on ion dynamics in a low-power magnetic nozzle thruster. *Plasma Sources Science & Technology*, *29*(4), 45002. https://doi.org/10.1088/1361-6595/ab74b6

[33] Wachs, B. & Jorns. B. (2018). Effect of Background Pressure on Ion Dynamics in an Electron Cyclotron Resonance Thruster. *2018 Joint Propulsion Conference*. https://doi.org/10.2514/6.2018-4585

[34] Jarrige, J., Elias, P., Cannat, F., & Packan, D. (2013). Performance Comparison of an ECR Plasma Thruster using Argon and Xenon as Propellant Gas. Presented at the 33rd International Electric Propulsion Conference, The George Washington University, Washington, D.C.

[35] Hallouin, & Mazouffre, S. (2020). Far-Field Plume Characterization of a 100-W Class Hall Thruster. *Aerospace*, *7*(5), 58. https://doi.org/10.3390/aerospace7050058

[36] Polarization Measurements. (n.d.) Antenna Theory. Retrieved March 04, 2022, from https://www.antenna-theory.com/

[37] Vialis, Jarrige, J., Aanesland, A., & Packan, D. (2018). Direct Thrust Measurement of an Electron Cyclotron Resonance Plasma Thruster. *Journal of Propulsion and Power*, *34*(5), 1323–1333. https://doi.org/10.2514/1.B37036

[38] Seshan, K. (2012). *Handbook of thin film deposition techniques, processes, and technologies / edited by Krishna Seshan.* (3rd ed..). William Andrew.

[39] Sputtering Yields. (n.d.) Angstrom Sciences. Retrieved March 06, 2022, from https://www.angstromsciences.com/sputtering-yields

[40] Zoerb, K., Williams, J., Williams, D., & Yalin, A. (2005). Differential Sputtering Yields of Refractory Metals by Xenon, Krypton, and Argon Ion Bombardment at Normal and Oblique Incidences. *Presented at the 29th International Electric Propulsion Conference.* Princeton University.

[41] Staab, D., Frey, A., & Garbayo, A., Shadbolt, L., Fabris, A., Gurciullo, A., Grondein, P., Moloney, R., Faircloth, D., & Lawrie, S. (2018). AQUAJET: An Electrodeless ECR Water Thruster.